PROCEEDINGS OF THE

97 EUROPEAN STUDY GROUP WITH INDUSTRY (97ESGI)

Santiago de Compostela, November 11 - 14, 2013

Editors

Alfredo Bermúdez de Castro López-Varela
Wenceslao González Manteiga
Peregrina Quintela Estévez
University of Santiago de Compostela and Technological Institute for Industrial Mathematics
alfredo.bermudez@usc.es; wenceslao.gonzalez@usc.es; peregrina.quintela@usc.es

José Antonio Vilar Fernández
University of A Coruña
jose.vilarf@udc.es

PROCEEDINGS OF THE

97 EUROPEAN STUDY GROUP WITH INDUSTRY (97ESGI)

The 97 ESGI was co-organized by the Spanish Network for Mathematics & Industry (math-in) and the Technological Institute for Industrial Mathematics (ITMATI).

The 97 ESGI was co-sponsored by Teknova through a project funded by the Norwegian government.

Index

Introduction **5**

Electric scale-up for a slag heating furnace **7**

Svenn Anton Halvorsen, Teknova AS
Dolores Gómez and Alfredo Bermúdez de Castro, University of Santiago de Compostela and ITMATI

Process models for the production of Microalumina **33**

Svenn Anton Halvorsen, Teknova AS
José Luis Ferrín and Alfredo Bermúdez de Castro, University of Santiago de Compostela and ITMATI

Designing an optimal network measurement sensors for monitoring geographical renewable resource **53**

Martín Gastón, CENER
Manuel Febrero, University of Santiago de Compostela and ITMATI

Acknowledgements **63**

Introduction

The 97 European Study Group with Industry (97 ESGI), held in Santiago de Compostela from 11 -14^{th} November 2013, was co-organized by the Technological Institute for Industrial Mathematics (ITMATI) and the Spanish Network for Mathematics & Industry (math-in).

Initiated in Oxford in 1968, Study Groups with Industry provide a forum for industrial scientists to work alongside academic mathematicians on problems of direct industrial relevance.

The success of the ESGI lies in its unique format which has been copied around the world, and which allows Mathematicians to work on reduced groups to study problems presented by industry. These problems arise from any economic sector thanks to the versatility of Mathematics.

The objective is to present the capabilities of Mathematics and its applicability in a large part of the challenges and needs that industry presents. It aims to bring small, medium and large companies a technology with great potential, used by highly qualified researchers and which does not require large investments to use.

Therefore, collaboration between industry experts and researchers is key to address technological innovation issues by using successful mathematical techniques. ESGI contributes to the promotion of mathematics and helps companies to use Mathematics to improve their processes.

The objectives set to achieve at the ESGI are:

- find solutions and insights into existing industrial problems;
- establish lasting and productive working links between applied mathematicians researchers and industry;
- propose new lines of research based on business challenges;
- reinforce the importance of mathematics in industry and the incorporation of mathematics to companies; and
- stimulate greater awareness in the wider community of the power of mathematics in providing solution paths to real-world problems.

Finally, it should be pointed out that 53 researchers, students, professors and company technicians contributed to a successfull 97 ESGI.

Santiago de Compostela on 14^{th} November, 2014

Members of the Scientific Committee:

- Alfredo Bermúdez de Castro López-Varela, Professor of the Department of Applied Mathematics at the University of Santiago de Compostela. Member of the Management board of math-in and member of the Technical Scientific Committee of ITMATI.
- Wenceslao González Manteiga, Professor of the Department of Statistics and Operations Research at the University of Santiago de Compostela. Member of the Governing Council of ITMATI.
- Peregrina Quintela Estévez, Professor of the Department of Applied Mathematics at the University of Santiago de Compostela. President of math-in and Director of ITMATI.
- José Antonio Vilar, Professor of the Department of Mathematics at the University of A Coruña.

Electric scale-up for a slag heating furnace

Academic Coordinators Alfredo Bermúdez de Castro and Dolores Gómez
University University of Santiago de Compostela and Technological Institute for Industrial Mathematics

Business Coordinator Svenn Anton Halvorsen
Company Teknova AS

Specialist Rafael Vázquez Hernández
Company Istituto di Matematica Applicata e Tecnologie Informatiche, Italy

Team Vincent Cregan (Centre de Recerca Matemàtica. Autonomous University of Barcelona), Francisco Pena (University of Santiago de Compostela and Technological Institute for Industrial Mathematics), Ángel Rial (University of Santiago de Compostela), Rune Schlanbusch (Teknova AS)

Electric scale-up for a slag heating furnace

Alfredo Bermúdez[*], *Vincent Cregan*[†], *Dolores Gómez*[‡], *Ángel Rial*[§], *Rafael Vázquez*[¶], *Svenn Anton Halvorsen*[‖]

Abstract

The aim of this study group is to contribute to the mathematical modelling and numerical simulation of a slag heating furnace. Two parallel studies were performed; one on numerical simulation of the process using a Finite Element Method software, while the other focused on non-dimensional thermal analysis of an electrode. Both studies provided preliminary results which are important stepping stones for a broad understanding of process relevant issues related to scale-up.

Keywords | electric slag heating; eddy-currents; nondimensional heat model

AMS classification | 35Q61, 65N30

1. Introduction

Teknova AS is a research institute for science and technology established in 2007 in the southern part of Norway. Among its primary objectives is to create a bond between the University of Agder, Agder Research, and the industry and commerce in the region and outside.

Recently, Teknova, in cooperation with several business and research partners, started a project funded with 3 million NOK (around 375 000 EUR) by the Regional Research Fund Agder. The project focuses on efficient development of metallurgical processes from laboratory to pilot scale through mathematical modelling tools and methods that safeguard the critical process capabilities during scale-up. The research is performed in close cooperation

[*]Universidade de Santiago de Compostela and ITMATI; alfredo.bermudez@usc.es
[†]Centre de Recerca Matemática. Universitat Autónoma de Barcelona; vcregan@crm.cat
[‡]Universidade de Santiago de Compostela and ITMATI; mdolores.gomez@usc.es
[§]Universidade de Santiago de Compostela; angel.rial@usc.es
[¶]Istituto di Matematica Applicata e Tecnologie Informatiche; vazquez@imati.cnr.it
[‖]Teknova AS; sah@teknova.no

with researchers in production companies, and is based on cases provided by the industry itself.

The industrial project partners have excellent facilities for piloting of metallurgy and other processing. The companies are members of the Eyde-network that was established as an important cluster organization and motor for industrial development in South-Norway in 2007. Currently, the cluster companies are establishing the Eyde Innovation Centre which will constitute the core of their common research activities. Teknova cooperates closely with the Eyde cluster and intends, among others, to supply relevant mathematical models, simulations tools and know-how for proper scale-up.

The problem presented to the ESGI 97 lies in this context and it is related to the electric scale-up for a slag heating furnace. A more detailed description is given in the next section.

2. Challenge description

Consider a possible slag process where the slag is more heavy than the metal. Consider a cylindrical reactor with side electrodes. For an experimental lab/pilot furnace a four electrode system with power control of two electric circuits is considered, compared to a three-phase alternative. For an industrial or large pilot, only a three-phase system seems appropriate. A schematic side-view of a reactor electrode is given in Fig. 1.

The focus of the study group was on the electrical part of a possible reactor and how to do a proper electrical scale-up. More precisely,

- Possible issues/problems going from a four-electrode system to three-phase electrodes.
- How to scale up the power for a three-phase reactor from typical lab scale, via pilot, to small industrial scale.

The group split into two teams examining different aspects of the problem. On one hand, the mathematical modelling and numerical simulation of the electromagnetic process. On the other, the statement of a nondimensional model dealing with the thermal phenomena.

3. Study of the electromagnetic problem

3.1. The time-harmonic eddy currents model

To calculate the electromagnetic field we must solve Maxwell's equations. Since the electrodes are supplied with a sinusoidal current and the medium is assumed to be magnetically linear, the time harmonic approach is used. Thus,

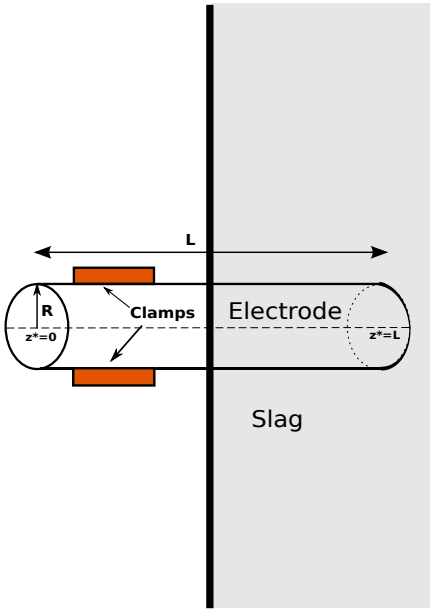

Figure 1: Close-up of one of the reactor electrodes.

we can consider that all fields vary harmonically with time on the form

$$\mathcal{F}(\mathbf{x}, t) = \mathrm{Re}\,[\mathrm{e}^{i\omega t}\,\mathbf{F}(\mathbf{x})], \tag{1}$$

where t is time, $\mathbf{x} \in \mathbb{R}^3$ is the spatial variable, i is the imaginary unit, $\mathbf{F}(\mathbf{x})$ is the complex amplitude of field $\mathcal{F}$ and ω is the angular frequency, $\omega = 2\pi f$, f being the frequency of the alternating current.

Moreover, in the low-frequency harmonic regime, the term in Ampere's law including the electric displacement can be neglected (see, for instance, reference [4]).

Under these assumptions, the Maxwell's equations reduce to the so-called *eddy current* model

$$\mathbf{curl}\,\mathbf{H} = \mathbf{J}, \tag{2}$$

$$i\omega\mathbf{B} + \mathbf{curl}\,\mathbf{E} = \mathbf{0}, \tag{3}$$

$$\mathrm{div}\,\mathbf{B} = 0, \tag{4}$$

to which we have to add the data of the intensity current, I, flowing in the electrodes. Equations (2)-(4) hold on the whole space $\mathbb{R}^3$. The vectorial fields $\mathbf{H}$, $\mathbf{J}$, $\mathbf{B}$ and $\mathbf{E}$ are the complex amplitudes associated with the magnetic field, the current density, the magnetic induction and the electric field, respectively.

The system above needs to be completed by the constitutive relation

$$\mathbf{B} = \mu\mathbf{H}, \tag{5}$$

which take into account material properties through their magnetic permeability μ. We also need Ohm's law

$$\mathbf{J} = \sigma \mathbf{E}, \tag{6}$$

where σ denotes the electric conductivity, which is assumed to be a positive constant in conductors and null in dielectrics.

We notice that, since $\omega \neq 0$, equation (4) follows from equation (3). As we will see later, equations (2) and (3) can be solved using a suitable formulation leading to $\mathbf{H}$ in the whole domain and $\mathbf{J}$ in conductors. Then, $\mathbf{E}$ can be uniquely determined in conductors by $\mathbf{E} = \mathbf{J}/\sigma$. In this case, solving for $\mathbf{E}$ in the dielectrics is not required since it is not relevant for this problem.

To solve the equations above, we restrict them to a simply connected 3D bounded domain Ω consisting of two disjoint parts, Ω_{C} and Ω_{D}, occupied by conductors (the slag and electrodes) and dielectric (air), respectively (see Fig. 2). The domain Ω is assumed to have a Lipschitz-continuous connected boundary Γ. We denote by $\Gamma_{\mathbf{C}}$ and Γ_{D} the open surfaces such that $\bar{\Gamma}_{\mathrm{C}} := \partial\Omega_{\mathrm{C}} \cap \Gamma$ is the outer boundary of the conducting domain and $\bar{\Gamma}_{\mathrm{D}} := \partial\Omega_{\mathrm{D}} \cap \Gamma$ that of the dielectric domain. We also denote by $\mathbf{n}$ a unit normal vector to a given surface.

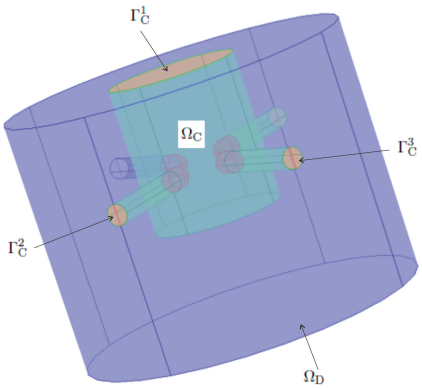

Figure 2: Sketch of the domain and nomenclature used in the mathematical model.

We assume that the outer boundary of the conductor $\partial\Omega_{\mathrm{C}} \cap \Gamma$ has L disjoint connected components $\Gamma_{\mathbf{C}}^n$, being the closure of open surfaces of two types: surfaces where the current intensity is prescribed (for instance $\Gamma_{\mathbf{C}}^2$ or $\Gamma_{\mathbf{C}}^3$ in Fig. 2), or surfaces where the potential is given (boundary $\Gamma_{\mathbf{C}}^1$ in Fig. 2). We denote $\Gamma_{\mathbf{C}} := \Gamma_{\mathbf{C}}^1 \cup \cdots \cup \Gamma_{\mathbf{C}}^L$. Notice that for this particular problem $L = 4$ or 5 depending on whether we consider 3 or 4 electrodes.

We have to complete the model with suitable boundary conditions. Let us consider the following ones:

$$\mathbf{E} \times \mathbf{n} = \mathbf{0} \quad \text{on } \Gamma_{\mathbf{C}}, \tag{7}$$

$$\mu \mathbf{H} \cdot \mathbf{n} = 0 \quad \text{on } \Gamma. \tag{8}$$

Condition (7) means that the electric current enters domain Ω perpendicular to the boundary whereas condition (8) implies that the magnetic field is tangential to the boundary.

Let us suppose that the boundary data consist of the voltage V_n, for $n = 1, \ldots, \widehat{L}$, and the input current intensities through each surface $\Gamma_{\mathbf{C}}^n$, I_n, for $n = \widehat{L}+1, \ldots, L$. We notice that the latter can be written as

$$\int_{\Gamma_{\mathbf{C}}^n} \mathbf{J} \cdot \mathbf{n} \, \mathrm{d}A = \mathrm{I}_n, \quad n = \widehat{L}+1, \ldots, L.$$

We summarize the strong problem defined in Ω to be solved:

$$i\omega \mathbf{B} + \mathbf{curl}\, \mathbf{E} = \mathbf{0}, \tag{9}$$

$$\mathbf{curl}\, \mathbf{H} = \mathbf{J}, \tag{10}$$

$$\operatorname{div} \mathbf{B} = 0, \tag{11}$$

$$\mathbf{B} = \mu \mathbf{H}, \tag{12}$$

$$\mathbf{J} = \sigma \mathbf{E}, \tag{13}$$

$$\mathbf{E} \times \mathbf{n} = \mathbf{0} \quad \text{on } \Gamma_{\mathbf{C}}, \tag{14}$$

$$\mu \mathbf{H} \cdot \mathbf{n} = 0 \quad \text{on } \Gamma, \tag{15}$$

$$\mathrm{V} = \mathrm{V}_{\mathrm{C}}^n \ \text{ on } \Gamma_{\mathbf{C}}^n, \ n = 1, \ldots, \widehat{L}, \tag{16}$$

$$\int_{\Gamma_{\mathbf{C}}^n} \mathbf{J} \cdot \mathbf{n} \, \mathrm{d}A = \mathrm{I}_n, \quad n = \widehat{L}+1, \ldots, L. \tag{17}$$

3.2. Magnetic vector potential/scalar electric potential formulation

Many formulations and finite element techniques to solve eddy current problems in three dimensional bounded domains can be found in the literature (see [1, 3]. Here, we have chosen that based on the scalar and the magnetic vector potential.

Firstly, from (11), (15) and [6, Theorem 1.3.6] we deduce the existence of a vector field $\mathbf{A} \in \mathbf{H}(\mathbf{curl}, \Omega)$ called magnetic vector potential such that

$$\mathbf{curl}\, \mathbf{A} = \mathbf{B} \text{ in } \Omega, \tag{18}$$

$$\operatorname{div} \mathbf{A} = 0 \text{ in } \Omega, \tag{19}$$

$$\mathbf{A} \times \mathbf{n} = \mathbf{0} \text{ on } \Gamma. \tag{20}$$

The latter equality guarantees boundary condition (15) (see [2])

By replacing (18) in (9) we obtain

$$\mathbf{curl}(i\omega\mathbf{A}+\mathbf{E})=\mathbf{0} \text{ in } \Omega,$$

and then, in particular, there exists a scalar potential V such that

$$i\omega\mathbf{A}+\mathbf{E}=-\operatorname{grad}\mathrm{V} \text{ in } \Omega. \tag{21}$$

Therefore, the magnetic and electric fields can be written in terms of these potentials as follows:

$$\mathbf{E}=-i\omega\mathbf{A}-\operatorname{grad}\mathrm{V},$$
$$\mathbf{H}=\frac{1}{\mu}\,\mathbf{curl}\,\mathbf{A}.$$

From (14) and (20) we deduce

$$\operatorname{grad}_\Gamma \mathrm{V}:=\mathbf{n}\times\operatorname{grad}\mathrm{V}\times\mathbf{n}=-\mathbf{n}\times\mathbf{E}\times\mathbf{n}=\mathbf{0} \quad \text{on } \Gamma_{\mathbf{C}},$$

which implies that V must be constant on each connected component of $\Gamma_{\mathbf{C}}$.

From (10), (12), (13) and (21) we deduce

$$\sigma(i\omega\mathbf{A}+\operatorname{grad}\mathrm{V})+\mathbf{curl}(\frac{1}{\mu}\,\mathbf{curl}\,\mathbf{A})=\mathbf{0} \text{ in } \Omega. \tag{22}$$

We notice that, since $\sigma=0$ in Ω_{D}, we only need to compute V in Ω_{C}.

Finally, from (13) and (21), boundary conditions (17) become

$$\int_{\Gamma_{\mathbf{C}}^n}\sigma(i\omega\mathbf{A}+\operatorname{grad}\mathrm{V})\cdot\mathbf{n}\,\mathrm{dS}=-\mathrm{I}_n, \quad n=\widehat{L}+1,\dots,L. \tag{23}$$

Summarizing, the problem to be solved reads as follows:

Given complex numbers $\mathrm{V}_{\mathrm{C}}^n$, $n=1,\dots,\widehat{L}$ *and* I_n, $n=\widehat{L}+1,\dots,L$, *find a vector field* $\mathbf{A}$ *defined in* Ω, *and a scalar field* V *defined in* Ω_{C} *and constant on* $\Gamma_{\mathbf{C}}^n$, $n=\widehat{L}+1,\dots,L$, *such that*

$$\sigma(i\omega\mathbf{A}+\operatorname{grad}\mathrm{V})+\mathbf{curl}(\frac{1}{\mu}\,\mathbf{curl}\,\mathbf{A})=\mathbf{0} \text{ in } \Omega, \tag{24}$$
$$\operatorname{div}\mathbf{A}=0 \text{ in } \Omega, \tag{25}$$
$$\mathbf{A}\times\mathbf{n}=0 \text{ on } \Gamma, \tag{26}$$
$$\sigma(i\omega\mathbf{A}+\operatorname{grad}\mathrm{V})\cdot\mathbf{n}=0 \text{ on } \partial\Omega_{\mathrm{C}}\setminus\Gamma_{\mathbf{C}}, \tag{27}$$
$$\mathrm{V}=\mathrm{V}_{\mathrm{C}}^n \text{ on } \Gamma_{\mathbf{C}}^n,\ n=1,\dots,\widehat{L}, \tag{28}$$
$$\int_{\Gamma_{\mathbf{C}}^n}\sigma(i\omega\mathbf{A}+\operatorname{grad}\mathrm{V})\cdot\mathbf{n}\,\mathrm{dS}=-\mathrm{I}_n,\ n=\widehat{L}+1,\dots,L. \tag{29}$$

For more details about this formulation, we refer the reader to [2].

3.3. Numerical simulation

In this section we present some results obtained from the numerical simulation of the problem. All FEM models, meshes and calculations were performed with the Comsol Multiphysics® 4.3 software, and in particular with the AC/DC module.

3.3.1 Geometry definition

A simple sketch of the reactor is composed by a pot, which contains the slag and a metal layer above the slag, and graphite electrodes. In order to deal with a more simple geometry, neither the pot nor the metal above the pot have been included. Instead, suitable boundary conditions have been considered. Thus, the domain reduces to the slag and to the electrodes carrying the electric current. We will consider the case of systems consisting of four or three electrodes. In order to perform suitable FEM numerical computations, this domain has been enclosed in a cylindrical artificial domain containing air around the device as illustrated in Fig. 3.

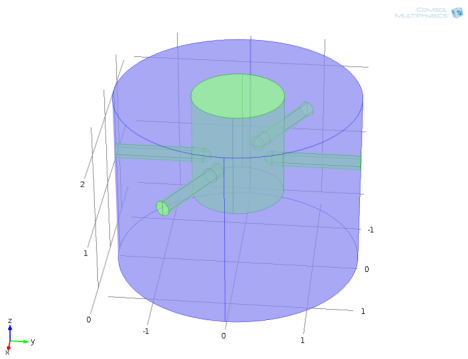

Figure 3: Computational domain for the four electrode configuration.

Moreover, the geometry has been constructed according to certain parameters that allow greater flexibility in the study. These parameters have been included in Fig. 4 and summarized in Table 1. In the four electrode system the angle θ between the electrodes has been set equal to 60^o, while for the alternative three electrode configuration they are disposed conforming an equilateral triangle.

The domain has been discretized into tetrahedral elements (see Fig. 5). As it is well-known, the quality of the mesh is crucial to obtain an accurate solution with a reduced number of elements and so a reasonable computational time. Thus, in electrode contact areas, where the current density is higher, the mesh density is refined (see Fig. 5). In the four-electrode case, the complete mesh consists of 174812 elements and 1354563 degrees of freedom, while for the

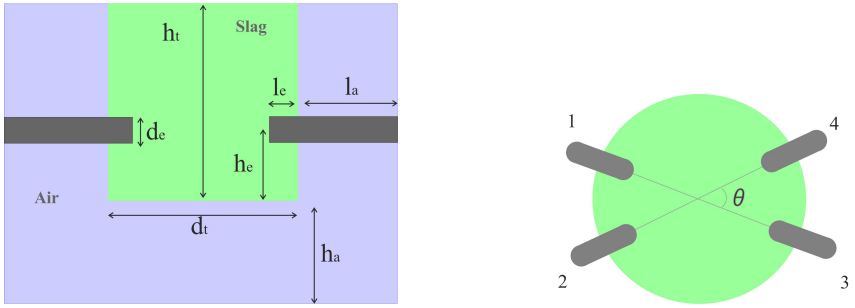

Figure 4: Sketch of a possible lab reactor. Parameters considered when constructing the geometry are detailed. Electrode pairs 1-3 and 2-4 are connected to different transformers.

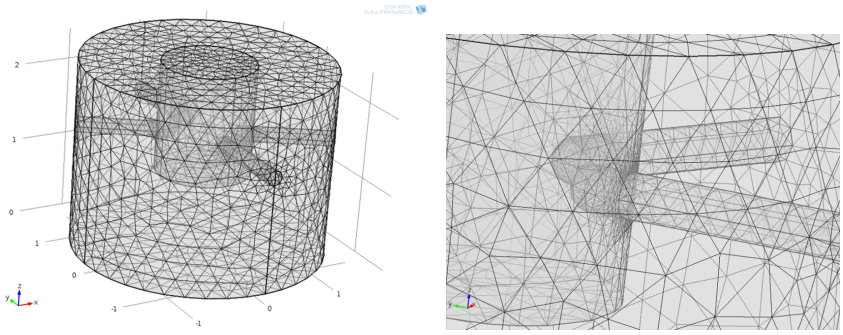

Figure 5: Mesh of the domain and detail in the electrodes contact areas.

three electrode configuration 132001 elements and 338087 degrees of freedom are considered. These meshes could probably be improved, but due to time constraints the working group did not consider this task. Even so, in the three-electrode case, we have compared the volumetric resistive losses obtained from different meshes to verify that the results are relatively accurate.

When working with alternating current, the electric current tends to become distributed within a conductor in such a way that the current density is higher near the surface of the conductor. This fact is called skin effect. The skin depth, δ is defined as the depth below the surface of the conductor at which the current density has fallen to 1/e from its value at the surface and in normal cases it is well approximated by the formula

$$\delta \simeq \sqrt{\frac{1}{\pi \mu \sigma f}}. \tag{30}$$

If the skin effect takes place, the skin depth is an important parameter to take into account when building the mesh if one wants to reproduce the field

Parameter	Description	Value (mm)
d_t	Tank diameter	1200
h_t	Tank height	1400
h_e	Electrode height from tank bottom	500
d_e	Electrode diameter	200
l_e	Electrode length in tank	150
l_a	Electrode length in air	1000
h_a	Air height below tank	1000

Table 1: Geometrical data for the simulations.

Parameter	Value
Frequency	50 Hz
Intensity	14000 A

Table 2: Operation conditions.

near the surface in an appropriate way. This is not the case in the actual computations, since skin effect is not relevant.

3.3.2 Operational conditions and physical parameters

The operational conditions chosen for the simulations are summarized in Table 2. These data and the data considering the geometry considered in the previous section, are reasonable for a potential pilot but do not correspond to actual plans. In the modelling example, the RMS value of the electrode currents is I = 14000 A. In the four data electrode configuration, every electrode pair has its own independent supply source (electrode pairs 1–3 and 2–4 are connected to different transformers). It means that the current trajectory in the slag can close only in the limitations of one source, so the currents flow from lower electrodes to opposite upper electrodes. In the three-electrode system, the electrode currents are the same with 120^o phase delay among them (three-phase current).

The input data given to Comsol Multiphysics® is the current density at the entry of each electrode which is computed as the quotient of the intensity and the input surface area. Thus, the current density is fixed and assumed to be homogeneously distributed on the input surface. Actually, induced currents contribute significantly to a non-uniform current distribution on this surface; this fact has not been considered in the present model due to software package constraints. Anyway, the error in current distribution only affects the part of the electrode close to its entry surface

Material	Rel. permeability	Conductivity (S/m)	Skin depth (mm)
Graphite	1	$24 \cdot 10^4$	145
Slag	1	700	2690
Air	1	0.00001	

Table 3: Values of physical properties of materials and skin depth at 50 Hz.

Table 3 lists the values assigned to the physical properties for the different materials and the skin depth in conductors at a frequency of 50 Hz.

We note that the electrical conductivity assigned to air is not zero, but rather very small. Again this was motivated by some restrictions derived from the model used by the numerical simulation in Comsol Multiphysics®. To the study group's best knowledge, the A-V formulation implemented in this software does not allow to solve for two different domains (conductor and air) simultaneously. This is the motivation for solving the problem as if the whole domain were a conducting domain, but assigning a small conductivity to the air. In fact setting $\sigma = 0$ in the air leads to a singular matrix, and therefore the algebraic system resulting from the FEM formulation cannot be solved.

3.3.3 Boundary conditions setting

One of the main difficulties in studying the eddy current problem in a bounded domain is defining appropriate boundary conditions. These conditions must be mathematically suitable for the problem to be well posed, but at the same time physically realistic in the sense of involving only data actually attainable in practical scenarios.

The boundary conditions have been summarized in Fig. 6. In all the exterior boundaries of the domain the `Magnetic Insulation` ($\mathbf{A} \times \mathbf{n} = \mathbf{0}$) boundary condition is imposed (default condition in Comsol Multiphysics®). This condition forces the field $\mathbf{B}$ to be tangential to the exterior boundaries, which with the cylindrical shape of the outer domain is a reasonable approximation to reality. Comsol Multiphysics® automatically applies this boundary condition through the exterior boundary of the domain. A supplementary boundary condition is needed in order to obtain a unique potential V. By default, Comsol Multiphysics® uses the `Electric Insulation` ($\mathbf{J} \cdot \mathbf{n} = \mathbf{0}$) boundary condition, which we impose on the boundary corresponding to the air. On the input surface of each electrode the current density is given by imposing a `Normal current density` boundary condition ($-\mathbf{n} \cdot \mathbf{J} = J_i$). In fact, following the model stated in Section 3.2, the data would be the intensity instead of the current density. As we have mentioned before, this would allow to compute the true current distribution in the electrodes instead of assuming that it is uniformly distributed on the entry surface. Finally, on the top part of

the reactor the potential is given via the `Electric potential` option and we choose V=0. The reason is that, on one hand, the potential is constant on this boundary and, on the other, the potential is defined up to a constant on each connected component of the conducting domain (see Section 3.2). Then, on one boundary of each connected component we can set V=0.

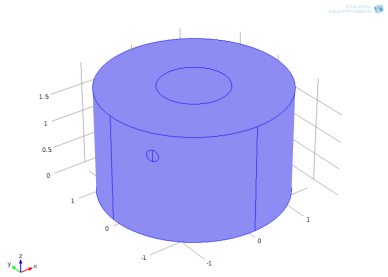

Magnetic insulation $\mathbf{A} \times \mathbf{n} = \mathbf{0}$

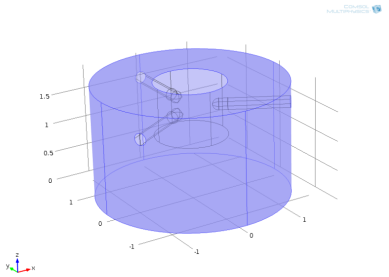

Electric insulation $\mathbf{J} \cdot \mathbf{n} = \mathbf{0}$

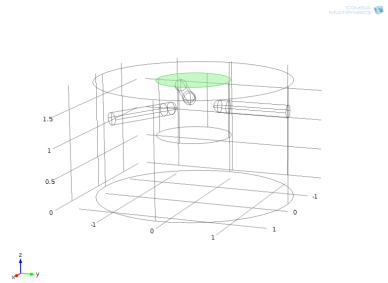

Electric potential V=0

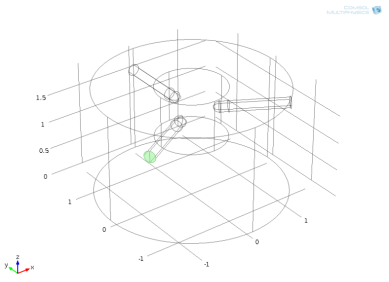

Normal current density $-\mathbf{n} \cdot \mathbf{J} = J_i$

Figure 6: Boundary conditions.

3.3.4 Numerical results for the four-electrode configuration

As mentioned in the previous section, for this case we have two separate electrode pairs supplied with 50 Hz AC single phase power.

In Figures 7 and 9 we show the Joule effect (or resistive losses) in the slag and electrodes, respectively, by using a slice plot. Figure 8 also shows the Joule effect in the slag but for demonstration purposes the maximum values of the field have been removed. In Figures 10, 11 and 12 a horizontal view has been employed to illustrate the Joule effect in the electrodes and slag. Figures 13 and 14 show the current density in the slag from different plane views.

From these pictures we deduce that the resulting current distribution within the slag is affected by the mutual influence of neighbouring electrodes of the magnetic fields, the so-called “proximity effect”. This effect is more obvious in the parts of the electrodes closer to the neighbouring electrodes. This is not

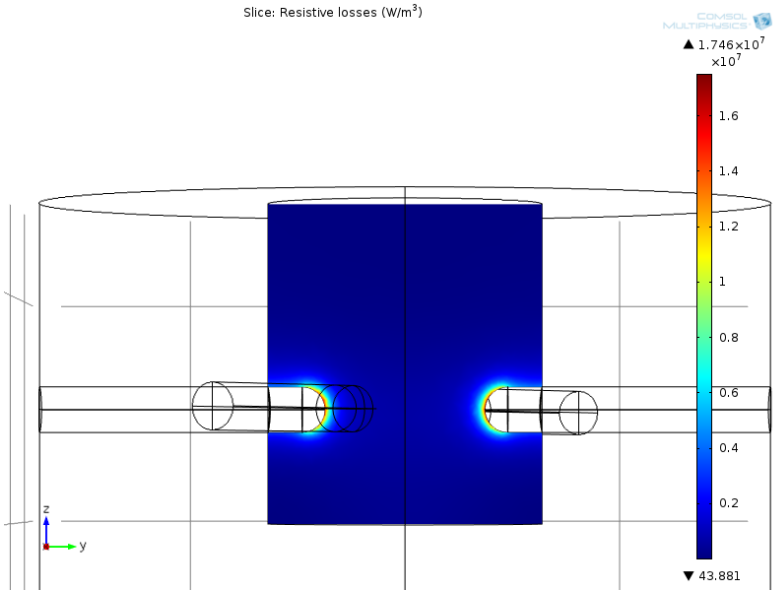

Figure 7: Joule effect (W/m^3) in the slag. yz view.

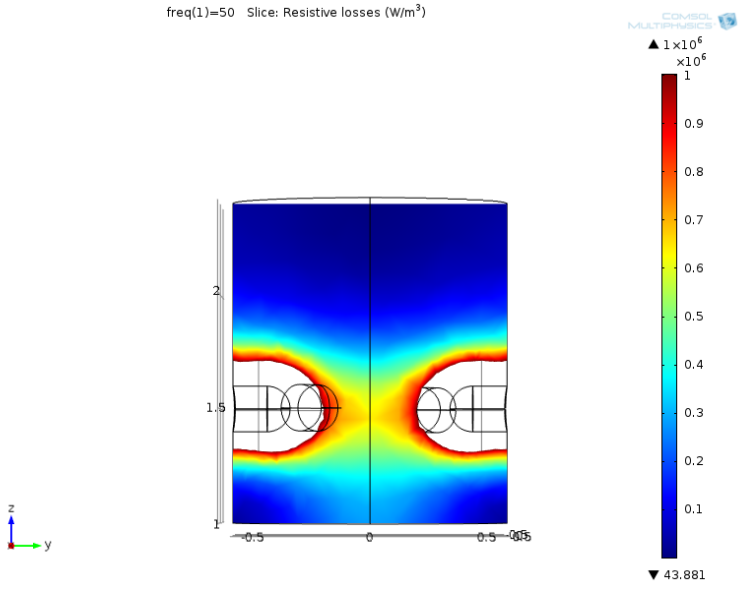

Figure 8: Joule effect (W/m^3) in the slag. Scale range. yz view.

the case in the three-electrode configuration (see Fig. 19) where the resistive losses are symmetrically distributed with respect to the meridional plane of the electrodes.

The aforementioned images were obtained from the values of the geomet-

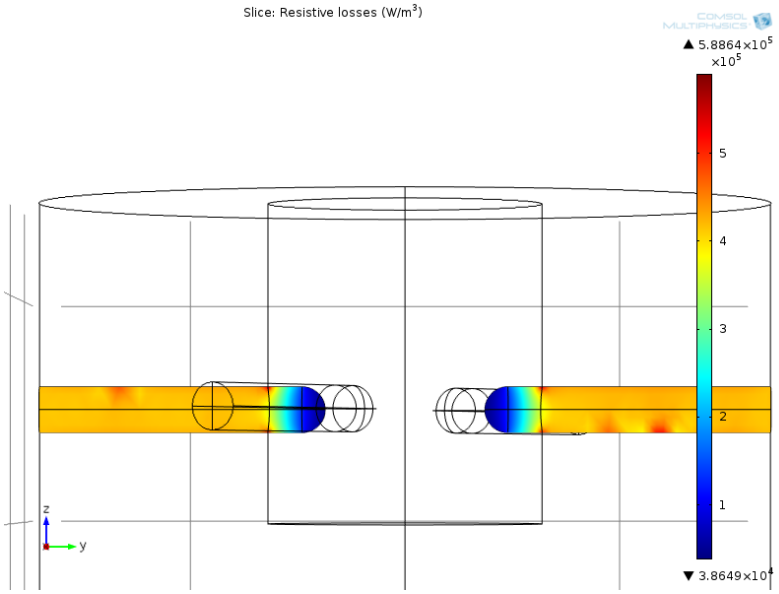

Figure 9: Joule effect (W/m^3) in the electrodes. yz view.

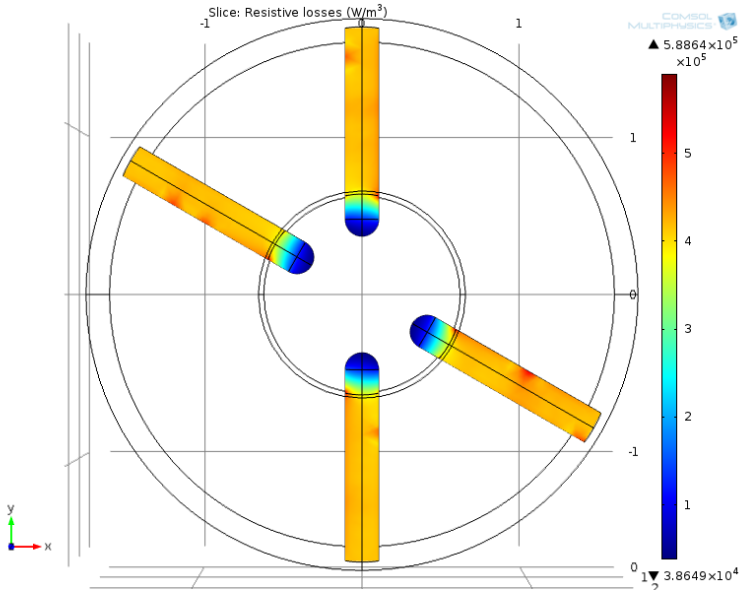

Figure 10: Joule effect (W/m^3) in the electrodes. Horizontal view

rical parameters stated in Table 1. In Fig. 14 we have also represented the current density by assuming that the parameter h_t is smaller than that of Fig. 13. This new computation represents a situation where the amount of slag in the pot is less than in the previous case. As we can see, in this case

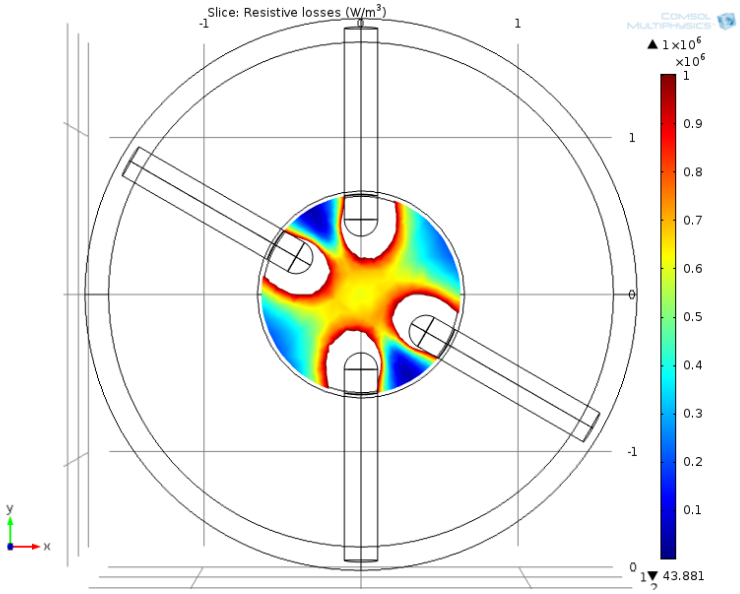

Figure 11: Joule effect (W/m^3) in the slag. Scale range. Horizontal view

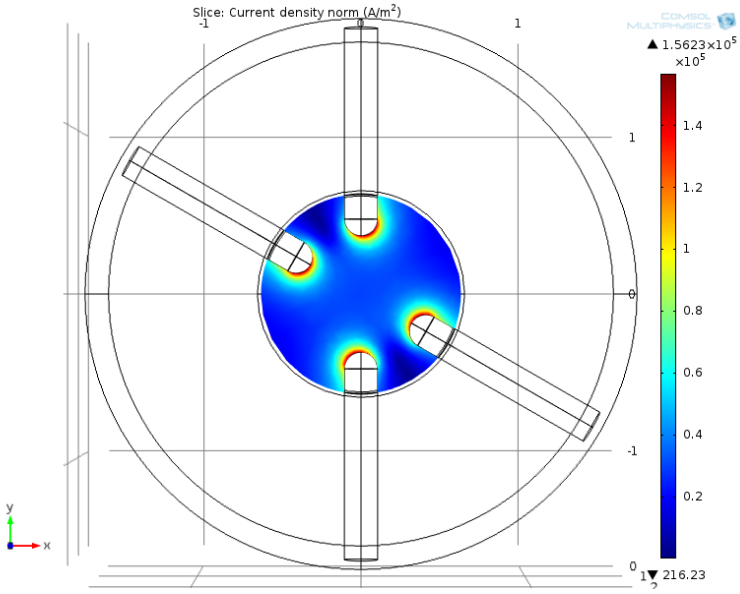

Figure 12: Current density norm (A/m^2) in the slag. Horizontal view

more current flows from the electrodes to the metal. Again, for presentation purposes we have removed the maximum values of the field.

Due to the geometry parametrization, as highlighted, these kinds of changes in geometry are quite easy to make.

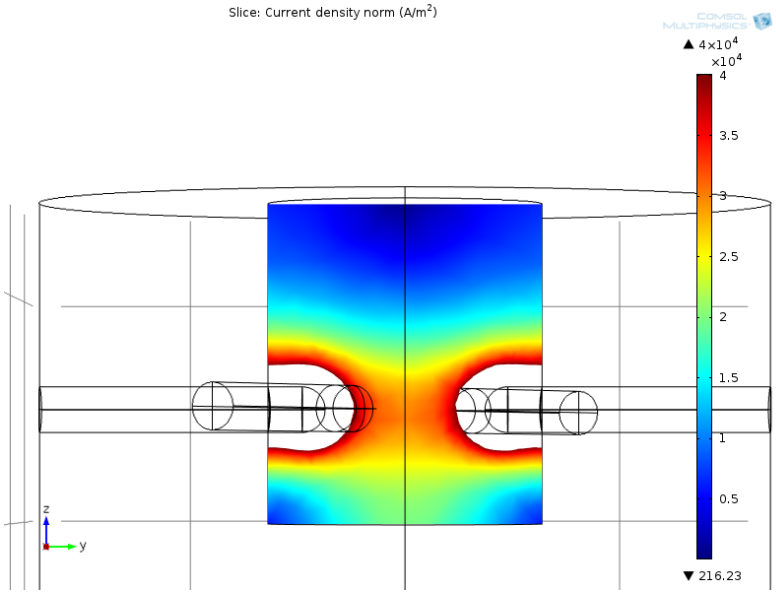

Figure 13: Current density norm (A/m^2) in the slag for h_t=1400 mm.

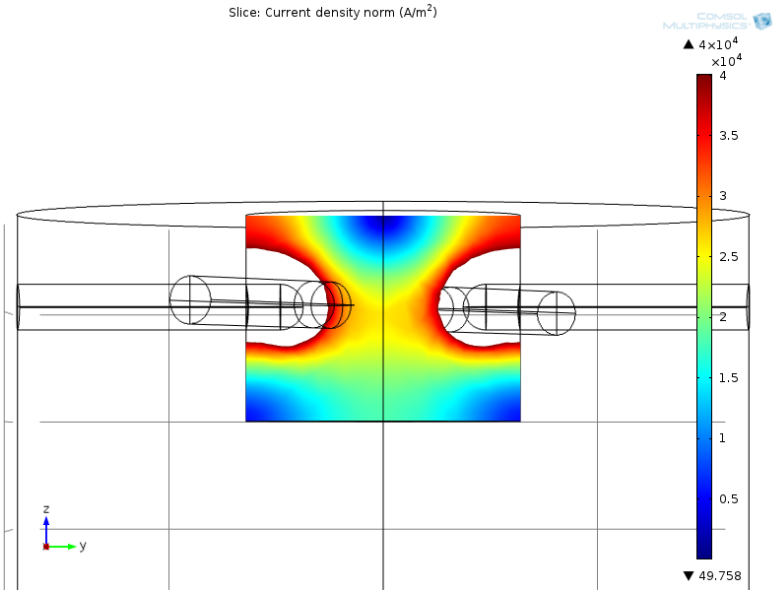

Figure 14: Current density norm (A/m^2) in the slag for h_t=900 mm.

3.3.5 Numerical results for the three-electrode configuration

In this section we show some of the results obtained from the numerical simulation of the three-electrode system (see Fig. 15) when considering the geo-

metrical and physical parameters summarized in Tables 2 and 3.

Since, we know the current intensity flowing through each electrode, we provide the RMS value of the alternating current and the phase in each electrode, with a counterclockwise advance of phase of 120^o. Recall that, as mentioned in Section 3.3.2, the data used in Comsol Multiphysics® is the current density.

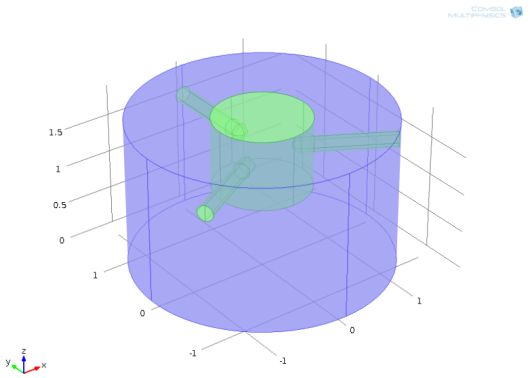

Figure 15: Domain with the three-electrode configuration.

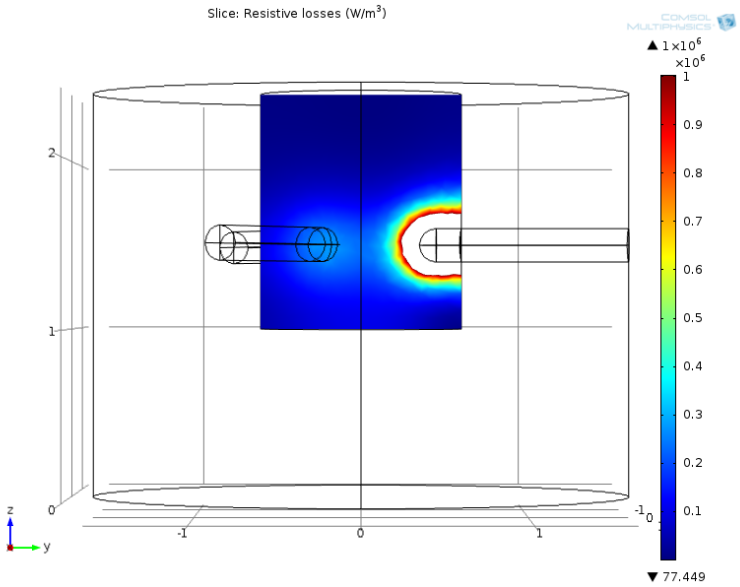

Figure 16: Joule effect (W/m^3) in the slag. Scale range

The Joule effect in the slag and in the electrodes is shown in Figures 16 and 17. In Fig. 16 we have removed the maximum values of the field for demonstration purposes. Figures 17 and 18 show the resistive losses in the

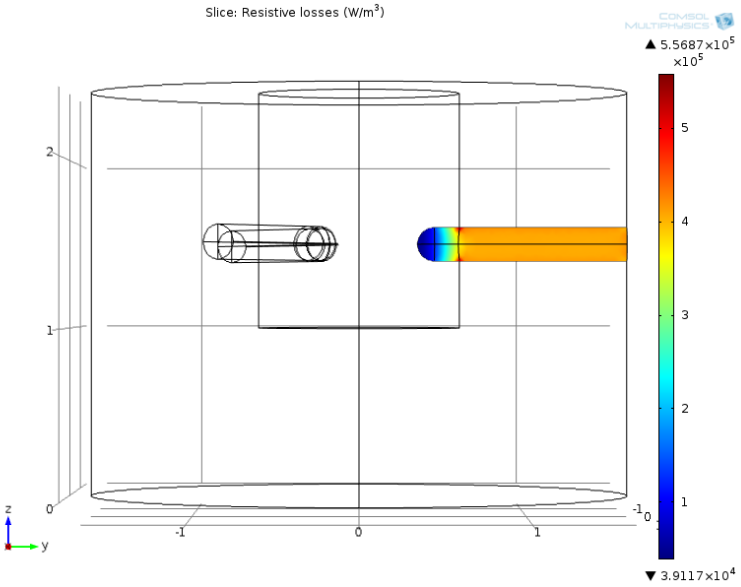

Figure 17: Joule effect (W/m^3) in the electrodes

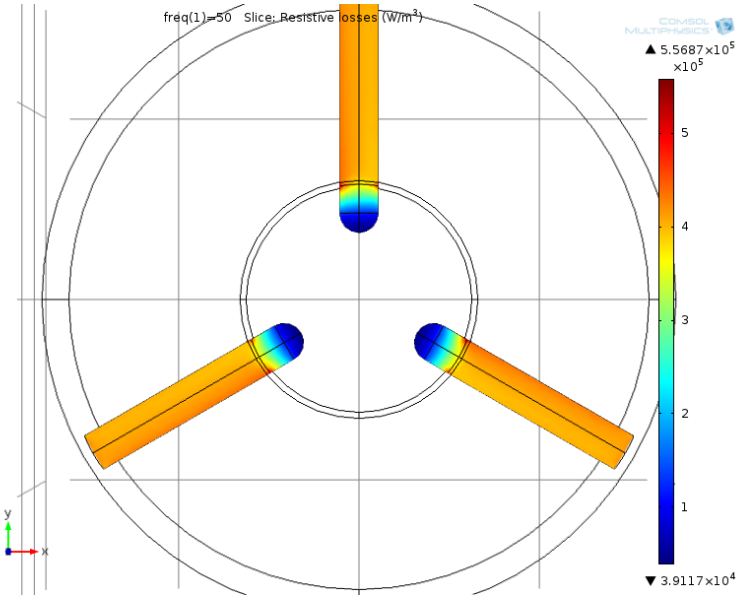

Figure 18: Joule effect (W/m^3) in the electrodes. Horizontal view

electrodes from different plane views; Fig. 19 shows resistive losses in the slag.

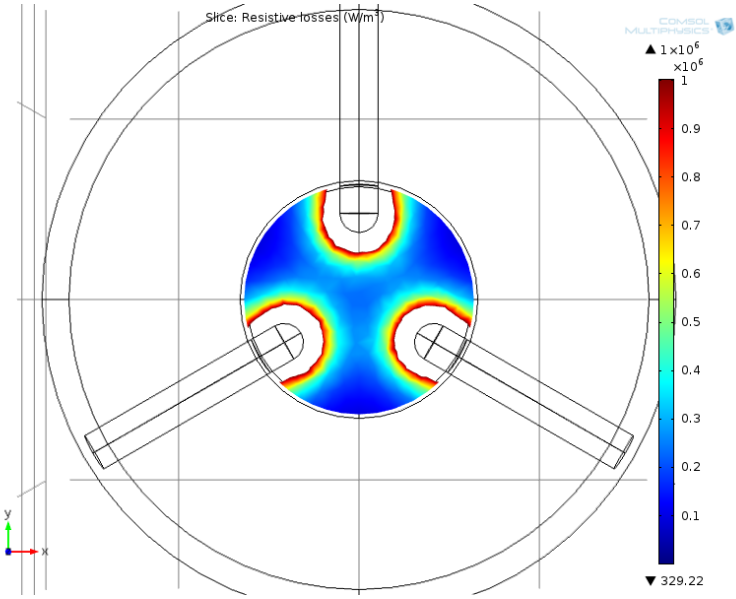

Figure 19: Joule effect (W/m^3) in slag. Scale range. Horizontal view

3.3.6 Some other results for the three-electrode system

In this section we show the resistive losses dissipated in the different parts of the three-electrode system while changing some of the geometrical parameters stated in Table 1. First, in Table 4 we consider different values for the parameters d_t and d_e, the diameter of the slag tank and the electrodes, respectively. We can deduce that, for a fixed value of d_e resistive losses in the slag and total losses increase with d_t. Analogously, for d_t fixed, the resistive losses in the slag and the total losses increase with d_e.

d_e (mm)	d_t=1200 (mm)	d_t=1400 (mm)	Region
200	3.83933E+04	3.85337E+04	electrodes
	3.10438E+05	3.28754E+05	slag
	1.02500E−02	1.10100E−02	air
	3.48831E+05	3.67288E+05	total
400	1.86131E+05	1.84224E+05	electrodes
	2.89721E+06	3.30162E+06	slag
	6.36200E−02	7.76100E−01	air
	3.08334E+06	3.48584E+06	total

Table 4: Resistive losses (W) in the three-phase system when changing d_e and d_t.

Region	h_t=1400 (mm)	h_t=2200 (mm)
electrodes	3.83933E+04	3.83974E+04
slag	3.10438E+05	3.11171E+05
air	1.02500E−02	1.07700E−02
total	3.48831E+05	3.49568E+05

Table 5: Resistive losses (W) in the 3 three-phase system when changing h_t.

Region	actual values (mm)	doubling values (mm)
electrodes	3.83933E+04	3.56964E+05
slag	3.10438E+05	2.86458E+06
air	1.02500E−02	1.04540E−01
total	3.48831E+05	3.22154E+06

Table 6: Resistive losses (W) in the three-phase system when doubling all geometrical parameters.

four electrode system	6.60223E+05
three electrode system	3.48831E+05

Table 7: Resistive losses (W) for the different configurations. Parameters values as in Table 1.

On the contrary, from Table 5, we deduce that as parameter h_t increases the resistive losses are practically the same.

In Table 6 we compare the losses when using the reference values stated in Table 1 with these values doubled. The losses are multiplied approximately by a factor of 10.

Table 7 summarizes the total resistive losses for both the four and three-electrode configurations, for geometrical and operation parameters detailed in Tables 1 and 2. These results show that, for the same parameter values, the three-phase system dissipates less power than the four-electrode one.

4. Thermal study for a single electrode

4.1. Mathematical model

In this section we consider the temperature evolution of one of the electrodes. Due to the physical description of the electrode we use a cylindrical coordinate system (r^*, θ^*, z^*) aligned with the cross section of the electrode, as shown in Fig. 1. We note that the * notation denotes dimensional variables. The length and radius of the electrode are denoted L and R, respectively. The electrode is aligned such that its axis coincides with the z-axis. The ends of the electrode are located at $z^* = 0$ and $z^* = L$.

The steady state temperature, T^*, in the electrode is modelled via the heat equation

$$\frac{1}{r^*}\frac{\partial}{\partial r^*}\left(k^*(T^*)r^*\frac{\partial T^*}{\partial r^*}\right)+\frac{1}{r^{*2}}\frac{\partial}{\partial \theta^*}\left(k^*(T^*)\frac{\partial T^*}{\partial \theta^*}\right)+\frac{\partial}{\partial z^*}\left(k^*(T^*)\frac{\partial T^*}{\partial z^*}\right)+Q=0\,, \tag{31}$$

where $k^*(T^*)$ is the temperature dependent thermal conductivity and Q is the Joule heating source term given by

$$Q = \frac{|J^2|}{2\sigma}\,, \tag{32}$$

where σ is the electrical conductivity and J is the amplitude current density [5]. Assuming a uniform temperature around the electrode, we neglect the θ^* dependence in the model, and hence, the θ^* partial derivative in (31) is ignored.

To complete the model, at the surface of the electrode we prescribe Newton's law of cooling boundary conditions of the form

$$-k^*(T^*)\frac{\partial T^*}{\partial n^*} = h(T^* - T_A)\,, \tag{33}$$

where h is the surface heat transfer coefficient and T_A is the ambient temperature of the surrounding medium. Inspection of Fig. 1 reveals that we require conditions at the ends of the electrode $z^* = 0$ and $z^* = L$. In addition, boundary conditions are needed at the curved surface of the electrode. These particular boundary conditions will depend on the surrounding medium, i.e., the slag or the outer casing of the reactor. Hence, there is a discontinuity in the boundary condition on the curved surface of the electrode. This suggests the use of a numerical method to solve for the temperature distribution of the electrode. We ignore this method here, and instead focus on a simple dimensional analysis.

4.2. Nondimensionalisation and dimensional analysis

The method of nondimensionalisation is applied to reduce the number of physical parameters, and simplify the model. We define the dimensionless variables

$$r^* = rR\,, \qquad z^* = zL\,, \qquad k^* = k_0 k\,, \qquad T^* = \Delta T T\,, \tag{34}$$

where k_0 is a reference thermal conductivity and the temperature scale ΔT is as yet unknown. Neglecting the θ dependence and substituting the dimensionless variables into (31) yields the dimensionless heat equation

$$\frac{1}{r}\frac{\partial}{\partial r}\left(k(T) r \frac{\partial T}{\partial r}\right) + \epsilon^2 \frac{\partial}{\partial z}\left(k(T)\frac{\partial T}{\partial z}\right) + \frac{|J^2|R^2}{2\sigma k_0 \Delta T} = 0\,, \tag{35}$$

where $\epsilon = R/L$ is the electrode aspect ratio. The radius and length of the electrode are 0.1m and 0.3m, respectively, and hence $|\epsilon^2 \ll 1$. Consequently, equation (35) can be simplified to

$$\frac{1}{r}\frac{\mathrm{d}}{\mathrm{d}r}\left(k(T) r \frac{\mathrm{d}T}{\mathrm{d}r}\right) + \frac{|J^2|R^2}{2\sigma k_0 \Delta T} + \mathcal{O}(\epsilon^2) = 0\,. \tag{36}$$

Assuming the thermal conductivity is temperature independent, (35) can be rewritten as

$$\frac{1}{r}\frac{\mathrm{d}}{\mathrm{d}r}\left(r \frac{\mathrm{d}T}{\mathrm{d}r}\right) + \frac{|J^2|R^2}{2\sigma k^* \Delta T} = 0\,, \tag{37}$$

where we have exploited $k^* = k k_0$. By assuming the electrical conductivity to be constant and large skin depth (30) compared to the electrode radius R, the current density J will not vary significantly over the cross-section of the electrode. Thus, the last term in (37) is approximately constant. The temperature variation is driven by the source term in (37) and so we choose the temperature scale to be

$$\Delta T = \frac{|J^2|R^2}{k^* 2\sigma}\,, \tag{38}$$

and hence (37) reduces to

$$\frac{1}{r}\frac{\mathrm{d}}{\mathrm{d}r}\left(r \frac{\mathrm{d}T}{\mathrm{d}r}\right) + 1 = 0\,. \tag{39}$$

The general solution to (39) is

$$T(r) = -\frac{r^2}{4} + C_0 \ln r + C_1\,, \tag{40}$$

where C_0 and C_1 are integration constants. Given the appropriate boundary conditions, (39) provides the temperature distribution in the electrode. The

unknown constants depend on whether the electrode surface is in thermal contact with the slag or the reactor casing.

Ignoring the precise details of (40) we return to the definition of the Joule effect heat source term. The current density for the cross section of the electrode is

$$J = \frac{\sqrt{2} I_{rms}}{A}\,, \tag{41}$$

where I_{rms} is the total rms current flowing through the electrode and $A = \pi R^2$ is the cross-sectional area of the electrode. Hence, the temperature scale given by (38) can be rewritten as

$$\Delta T = \frac{I_{rms}^2}{\pi^2 R^2 k^* \sigma}\,. \tag{42}$$

The above expression shows that for a fixed ΔT, the current I is proportional to the radius of the electrode.

5. Conclusions

The study group working in this problem focused on examining two different aspects: on one hand, the mathematical modelling and numerical simulation of the electromagnetic process; on the other, the statement of a nondimensional model dealing with the thermal phenomena.

Concerning the electromagnetic problem, a mathematical model has been proposed and some numerical computations performed. A parameterized code that can be used to compute the solution for different geometrical and physical parameters has been built using the Comsol Multiphysics® software. The preliminary computations show that the same dimensions of the furnace and same intensity, the three-phase system dissipates less power than a one-phase configuration.

We considered a thermal model for the temperature evolution of a single electrode. The dimensional analysis indicates a proportional relationship between the electrode radius and the current. A discontinuity in the surface temperature requires the use of an appropriate numerical simulation. In the future the thermal model should be coupled with the electromagnetic problem to obtain a complete description of the process.

The process taking place within the reactor is truly multi-physics, with couplings between heat transfer, chemical reactions and electrical phenomena. For a real study of the process a mathematical model including all these aspects should be considered. In this sense, the thermal dimensionless model proposed on the second part of this document is a first step in this direction.

References

[1] A. Alonso Rodríguez and A. Valli, *Eddy current approximation of Maxwell equations, ser. MS&A. Modeling, Simulation and Applications*, Springer-Verlag, Milan, Italia, vol. 4, 2010.

[2] A. Bermúdez, D. Gómez, P. Salgado, *Mathematical models and numerical simulation in electromagnetism*, Springer-Verlag, Milan, Italia, vol. 74, 2014.

[3] A. Bermúdez, R. Rodríguez, and P. Salgado, FEM for 3D eddy current problems in bounded domains subject to realistic boundary conditions. An application to metallurgical electrodes, *Computer Methods in Applied Mechanics and Engineering*, **12**, (2005) no. 1, pp. 67–114.

[4] A. Bossavit, *Computational electromagnetism*, Academic Press Inc., San Diego, CA, 1998.

[5] H. Fangohr, D.S. Chernyshenko, M. Franchin, T. Fischbacher, and G. Meier, Joule heating in nanowires, *Physical Review B* **84** (2011), no. 5, 054437.

[6] V. Girault, P.A. Raviart, *The finite element method for Navier-Stokes equations*, Springer-Verlag, New York, 1986.

Process models for the production of Microalumina

Academic Coordinator Alfredo Bermúdez de Castro and José Luis Ferrín
University University of Santiago de Compostela and Technological Institute for Industrial Mathematics

Business coordinator Svenn Anton Halvorsen
Company Teknova AS

Specialist Amable Liñán
University Polytechnic University of Madrid

Team Ibán Constenla (ITMATI), Saray Busto (University of Santiago de Compostela), Elena Vázquez (University of Santiago de Compostela), Colin Please (University of Oxford), María Bruna (University of Oxford), Tim Myers (Centre de Recerca Matemàtica)

Process models for the production of Microalumina

Alfredo Bermúdez[*], *José Luis Ferrín*[†], *Svenn Anton Halvorsen*[‡]

Abstract

The purpose of this Study Group is to contribute to the mathematical modelling of the processes underlying in the production of microalumina from aluminium droplets and Al-rich gas. The methodology deals with the combustion of aluminium to produce alumina and the subsequent nucleation to form microalumina particles.

Keywords | Combustion; Microalumina; Nucleation

AMS classification| 80A25

1. Problem approach by the Company

1.1. Introduction

In a project supported by the Research Council of Norway, Elkem Silicon Materials intends to make affordable, spherical micro/nano alumina (Al_2O_3) powder available for multiple industrial applications, in particular CA-cement, refractories and ceramics.

For silica-based refractories, Elkem has previously introduced a spherical micro/nano silica with good properties, resulting in improved flow of the refractory mix, better materials, longer lifetime and reduced consumption of refractory material. Due to softening, silica is precluded for high-temperature applications ($> 1500\ ^oC$). A similar micro/nano alumina does exist, but the price is prohibitive for refractories and many other potential applications.

A reasonably priced, spherical micro/nano alumina for use in high temperature refractories has been requested for a long time by the industry. The probable benefits of the product are widely accepted, but it is just not available.

[*]Universidade de Santiago de Compostela and ITMATI; alfredo.bermudez@usc.es
[†]Universidade de Santiago de Compostela and ITMATI; joseluis.ferrin@usc.es
[‡]Teknova AS; sah@teknova.no

Preliminary investigations by Elkem have revealed that the intended process is not easy to establish. Initial screening has, however, shown two possible production principles that should be further investigated.

A fundamental approach has been chosen where the two processes shall be described by mathematical models, which shall be verified by experiments. This will be an iterative process between modelling and experimental testing.

Provided successful initial testing, the most promising alternative will be followed up by further modelling, laboratory process design, and testing.

1.2. Atomising principle

In a process based on the atomising principle, aluminium droplets are first formed in an industrial atomiser. Then oxygen, air, or a controlled mixture of oxygen and inert gas is added either together with the atomising gas or somewhat downstream.

Aluminium combustion has been studied for years, as it has been added to propellants as an extra energy source. An overview is given by Beckstead[1]. Some points from this report:

- Aluminium burns in the gas phase.
- The Al-gas burns at some distance from the Al-droplet, up to some 10 droplet radii.
- Some intermediate products are $AlO_{(g)}$ and $Al_2O_{(g)}$.
- The (final) reaction product is liquid Al_2O_3 (melting point approximately 2050 řC).
- Combustion is controlled by the diffusion of fuel and oxidiser.
- Condensed alumina can deposit on an Al-droplet.
- Ignition occurs due to the failure of the protective layer of the Al_2O_3-shell surrounding an Al-droplet.
- Ignition temperature seems to be high, $\sim$ 2000-2100 K, but some researchers report far lower values for certain conditions, 1000-1300 K.

The ESGI discussions should concentrate on possible small scale experiments:

- Suitable conditions and requirements for safe, controlled Al-burning.
- Ignition considerations (preheating?).

If possible, the discussions may include.

- How to control the particle size.
- Micro models for creation and growth of alumina particles.

These topics will, however, be addressed for the fused process principle.

1.3. Fused principle

The fused principle consists of creating an Al-rich gas and then add oxygen to burn the gas. For the ESGI discussions we will assume that there is available a constant flow of a high temperature gas consisting of: $Al_{(g)}$, $AlO_{(g)}$, $Al_2O_{(g)}$, N_2, and CO. The temperature will be around 2000 ^{o}C, or higher.

From another project (carbothermic Al-process) it is known that an oxy-carbide slag can be formed by adding carbon to liquid alumina. When this slag is heated further, $Al_{(l)}$, $CO_{(g)}$, $Al_{(g)}$, $Al_2O_{(g)}$, and possibly also $AlO_{(g)}$, will be produced; the higher the temperature, the higher the fraction of Al-gases. Only gas will be produced at 2140 ^{o}C (see White *et al* [7]). Nitrogen can be added if it is beneficial to dilute the gas and other methods to produce the Al-rich gas can be considered.

For the ESGI discussions we will assume that a suitable gas production can be maintained. Oxygen or a mixture of O_2/N_2 is then added to the gas stream, or the gas may simply be transported to (possibly hot) air.

The focus for the ESGI discussions should be the burning process, including flame size and temperature, "condensation" into Al_2O_3 and the creation and growth of liquid Al_2O_3 particles. Some possible burning and condensation reactions are (see Beckstead[1]):

$$\begin{aligned} &Al_{(g)} + O_2 \rightarrow AlO + O, \\ &AlO + O_2 \rightarrow AlO_2 + O, \\ &2AlO + 1/2O_2 \rightarrow Al_2O_{3(l)}, \\ &Al_2O + O_2 \rightarrow Al_2O_{3(l)}, \\ &2AlO_2 \rightarrow Al_2O_{3(l)} + 1/2O_2. \end{aligned} \tag{1}$$

Alumina will "boil" around 4000 K according to the dissociation reaction (see Beckstead[1]):

$$Al_2O_{3(l)} \rightarrow 2AlO + 1/2O_2. \tag{2}$$

This reaction is strongly endothermic and will hence limit the flame temperature.

CO is stable at high temperatures and is not included as a reactant (see Beckstead[1]). NO_x gas species are likely to be formed if N_2 is present, but it is not required to be included in the ESGI treatment. NO_x is a problem that can be handled by available technology.

2. Mathematical model for the combustion of aluminium

Because aluminium has been added to propellants as an extra energy source, research on the combustion mechanism of burning aluminium has been an ongoing effort. Characteristics of aluminium combustion were summarised in the review by Beckstead[1].

The aim of this section is to contribute to the modelling of the combustion of individual aluminium droplets in their local gas environment, which results from the collective effects of all droplets in the domain. This will be done following the method of large activation energies used by Liñán[4] in his analysis of the ignition and extinction of diffusion flames, and applied in Liñán[5] for the vaporisation and combustion of droplets.

The analysis provides relations for the volumetric sources appearing in the gas phase description, and for the rates that determine the evolution of the size and temperature of the droplet.

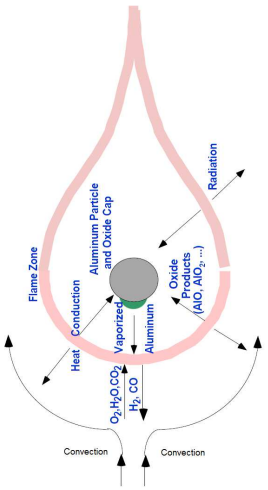

Figure 1: Scheme of the combustion process occurring around an aluminium droplet

There is a large variety of models for describing the combustion of a single aluminium droplet. For example, Beckstead [1] introduce a model (see Figure 1 for the physical interpretation), which has been developed to describe aluminium combustion in rocket motors. The kinetic mechanism in his model consists of surface reactions and gas phase reactions for the formation of the aluminium sub-oxides. The aluminium sub-oxides later react and condense to form liquid aluminium oxide. The path to condensation consists of two steps; a homogeneous gas phase reaction, followed by homogeneous condensation. The combustion mechanism accounts for a first kinetic step of the two-step

process, while the second step must be described with a condensation model. The reactions considered in the first step are:

Surface reactions:

$$\begin{aligned} &Al_{(l)} \rightarrow Al_{(g)}, \\ &Al_{(l)} + AlO_{(g)} \rightarrow Al_2O_{(g)}. \end{aligned} \tag{3}$$

Gas phase reactions:

$$\begin{aligned} &Al_{(g)} + O_2 \rightarrow AlO + O, \\ &AlO + O_2 \rightarrow AlO_2 + O, \\ &Al_{(g)} + CO_2 \rightarrow AlO + CO, \\ &Al_{(g)} + H_2O \rightarrow AlO + H_2, \\ &O + O + M \rightarrow O_2 + M, \\ &O + N_2 \rightarrow NO + N, \\ &N + O_2 \rightarrow NO + O. \end{aligned} \tag{4}$$

Dissociation reaction:

$$Al_2O_{3(l)} \rightarrow 2AlO + 1/2O_2. \tag{5}$$

Condensation reactions:

$$\begin{aligned} &2AlO + 1/2O_2 \rightarrow Al_2O_{3(l)}, \\ &2AlO + CO_2 \rightarrow Al_2O_{3(l)} + CO, \\ &2AlO + H_2O \rightarrow Al_2O_{3(l)} + H_2, \\ &Al_2O + O_2 \rightarrow Al_2O_{3(l)}, \\ &Al_2O + 2CO_2 \rightarrow Al_2O_{3(l)} + 2CO, \\ &Al_2O + 2H_2O \rightarrow Al_2O_{3(l)} + 2H_2, \\ &AlO_2 + AlO_2 \rightarrow Al_2O_{3(l)} + 1/2O_2. \end{aligned} \tag{6}$$

2.1. Gas phase

The above model is very complex. As a first step, in what follows we consider a simplified physicochemical model describing the combustion of an aluminium droplet. Firstly, we proceed with modelling the gas phase.

We have considered a simplified kinetic model consisting of the following physicochemical processes at the aluminium droplets (described graphically in Figures 2 and 3):

- Heterogeneous reaction:

  1 $\quad \mathrm{Al}_{(l)} \rightarrow \mathrm{Al}_{(g)} \quad +(q_1)$

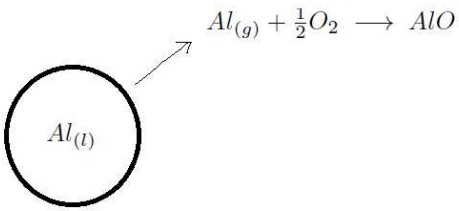

Figure 2: Kinetic scheme of the combustion of a single aluminium droplet

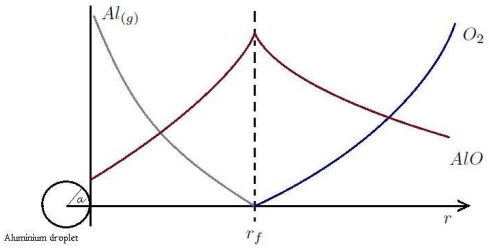

Figure 3: Phenomena occurring in the diffusion flame

- Gas phase oxidation reaction:
  2 $\quad \mathrm{Al}_{(g)} + 1/2\mathrm{O}_2 \rightarrow \mathrm{AlO} \quad +(q_2)$

- Condensation reaction:
  3 $\quad 2\mathrm{AlO} + 1/2\mathrm{O}_2 \rightarrow \mathrm{Al_2O_{3(l)}} \quad +(q_3)$

where q_i is the heat released in the i-th reaction per unit mass.

The aluminium droplet combustion model to be developed below has to be coupled with a gas phase model which establishes the mean field or local average conditions, of the gas where aluminium droplets are burnt. They are represented by mean field values, denoted by the index g, of the velocity, temperature and mass fractions of the gaseous mixture.

In order to obtain a simplified mathematical description of this combustion problem, let us assume the following hypotheses: all the diffusion coefficients D_i of chemical species are equal to D, Lewis number is equal to 1, so $k_T = \rho \mathrm{D} c_p$, Fick's law for the diffusion velocities and low Mach number (then, pressure can be assumed to be constant in the state equation). With these assumptions, equations considered for that turbulent mixture of reacting gases are: the

continuity and momentum conservation equations

$$\frac{\partial \rho_g}{\partial t} + \operatorname{div}(\rho_g \mathbf{v}_g) = f^m, \tag{7}$$

$$\frac{\partial (\rho_g \mathbf{v}_g)}{\partial t} + \operatorname{div}(\rho_g \mathbf{v}_g \otimes \mathbf{v}_g) + \nabla p - \operatorname{div}\left((\mu + \mu_t)(\nabla \mathbf{v}_g + \nabla \mathbf{v}_g^t) - \frac{2}{3}(\mu + \mu_t) \operatorname{div} \mathbf{v}_g \mathbb{I} - \frac{2}{3}\rho_g k \mathbb{I} \right) = \rho_g \mathbf{g}, \tag{8}$$

a turbulence model, for example the standard $k - \epsilon$ model

$$\mu_t = 0.09 \rho_g \frac{k^2}{\epsilon}, \tag{9}$$

$$\frac{\partial (\rho_g k)}{\partial t} + \operatorname{div}(\rho_g \mathbf{v}_g k) - \operatorname{div}\left[(\mu + \mu_t) \nabla k \right] = P_k - \rho_g \epsilon, \tag{10}$$

$$\frac{\partial (\rho_g \epsilon)}{\partial t} + \operatorname{div}(\rho_g \mathbf{v}_g \epsilon) - \operatorname{div}\left[\left(\mu + \frac{\mu_t}{1.3} \right) \nabla \epsilon \right] = 1.44 \frac{\epsilon}{k} P_k - 1.92 \frac{\epsilon^2}{k} \tag{11}$$

and the equations for species and energy conservation, given by

$$\mathcal{L}_g(Y^g_{O_2}) = f^m_{O_2} - \frac{16}{27} w_2, \tag{12}$$

$$\mathcal{L}_g(Y^g_{AlO}) = f^m_{AlO} + \frac{43}{27} w_2, \tag{13}$$

$$\mathcal{L}_g(Y^g_{Al}) = f^m_{Al} - w_2, \tag{14}$$

$$\mathcal{L}_g(h^g_T) = f^e + q_2 w_2 - \operatorname{div} \mathbf{q}_{rg}, \tag{15}$$

with f^m being the mass source per unit volume and time, w_2 the rate of the 2-th reaction and $\mathcal{L}_g$ the differential operator defined by

$$\mathcal{L}_g(u) = \frac{\partial (\rho_g u)}{\partial t} + \operatorname{div}(\rho_g u \mathbf{v}_g) - \operatorname{div}(\rho_g \mathcal{D} \nabla u). \tag{16}$$

In order to close the system, we need the state equation

$$\overline{p} = \rho_g \mathrm{R} T. \tag{17}$$

Since the activation energy of the gas phase oxidation reaction is very high, the Burke-Schumann procedure can be used, allowing us to simplify the analysis. Then the gas phase oxidation reaction can be considered as either frozen or occurring at infinitely fast velocity in a gaseous thin diffusion flame, at a distance r_f of the surface of the droplet as seen in Figure 4.

In the Burke-Schumann limit of infinite reaction rate, mass and energy conservation equations are complemented with the condition of non-coexistence of O_2 and $Al_{(g)}$. Then, the gas domain will be divided into two regions, Ω_O with oxygen and without aluminium, and Ω_A with aluminium but without

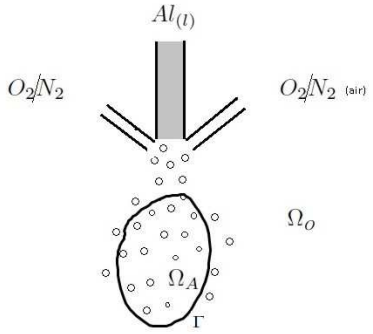

Figure 4: Diffusion flame

oxygen, separated by an infinitely thin boundary, Γ, where the diffusion flame is located.

In order to obtain equations without the gas phase reaction term we consider the following linear combinations of Shvab–Zeldovich type:

$$\begin{aligned} X_1^g &= Y_{O_2}^g - \frac{16}{27} Y_{Al}^g, \\ X_2^g &= Y_{AlO}^g + \frac{43}{27} Y_{Al}^g, \\ H^g &= h_T^g + q_2 Y_{Al}^g. \end{aligned}$$

Thus, we can obtain the following conservation equations, where the term (in general, nonlinear and stiff) associated to the gas phase reaction has been eliminated but including, however, homogenised sources coming from the gasification of the droplets:

$$\begin{aligned} \mathcal{L}_g(X_1^g) &= f_{O_2}^m - \frac{16}{27} f_{Al}^m, \\ \mathcal{L}_g(X_2^g) &= f_{AlO}^m + \frac{43}{27} f_{Al}^m, \\ \mathcal{L}_g(H^g) &= f^e + q_2 f_{Al}^m - \nabla \cdot \mathbf{q}_{rg}. \end{aligned}$$

Since Al and O_2 cannot coexist, due to the Burke-Schumann condition, then $X_1^g = Y_{O_2}^g - \frac{16}{27} Y_{Al}^g$ determines the region in which we are, namely,

1. If $X_1^g > 0 \Rightarrow$ Domain $\Omega_O \Rightarrow Y_{Al}^g = 0$

$$\begin{aligned} Y_{O_2}^g &= X_1^g, \\ Y_{AlO}^g &= X_2^g, \\ h_T^g &= H^g. \end{aligned}$$

2. If $X_1^g < 0 \Rightarrow$ Domain $\Omega_A \Rightarrow Y_{O_2}^g = 0 \ \ (\Rightarrow w_2 = 0)$

$$Y_{Al}^g = -\frac{27}{16} X_1^g,$$
$$Y_{AlO}^g = X_2^g - \frac{43}{27} Y_{Al}^g,$$
$$h_T^g = H^g - q_2 Y_A l^g.$$

2.2. Computing the sources from the liquid phase

Whereas we have considered an Eulerian description for the gas phase model, for the liquid phase we are going to consider a Lagrangian description. This is based on the assumption that the typical distance, d, between droplets of radius a verifies $d \gg a$. Thus, the liquid phase can be treated as a dispersed one and it allows us to use homogenisation techniques to describe the spray.

We need to know the droplet response in the mean local gas environment. If we restrict our attention to the case of low Peclet number, based on the relative velocity of the droplet to the local gas environment, then the effects of the motion of this ambient gas relative to the particle can be neglected, so that the mass fraction and temperature fields within the droplet and in its neighbourhood can be considered spheric-symmetrical. This is because the droplet is burning in a stagnant environment while surface tension effects keep the droplet spherical, when Peclet number is less than one.

Remark 2.1. *For large Peclet numbers and Weber numbers ($We = \rho_g v_g^2 a/\sigma$) of the order of 10 or larger, droplet deformation and break-up may arise.*

If we consider that consumption of liquid aluminium only takes place on the surface of the droplet through vaporisation reaction 1, then the evolution of the mass of an aluminium droplet, m_d, with the radial coordinate r and time t, is given by

$$\frac{dm_d}{dt} = -4\pi a^2 m_1'', \tag{18}$$

where $a(t)$ is the radius of the droplet and m_1'' is the mass gasified in the vaporisation reaction per unit area and time. Because of the hypothesis of sphericity of the droplets, equation (18) can be written as

$$\rho_l \frac{da}{dt} = -m_1'', \tag{19}$$

with ρ_l the density of the liquid aluminium.

In the same way, the evolution of the droplet temperature, T_d, is obtained from the equation:

$$m_d c_l \frac{dT_d}{dt} = 4\pi a^2 (q_p'' + q_r'') + 4\pi a^2 q_1 m_1'', \tag{20}$$

where q_1 is the heat of vaporisation per unit mass and q_p'' and q_r'' are the heat fluxes by conduction and radiation, respectively, given by

$$q_p'' = k\frac{dT}{dr}_{|_{r=a^+}},$$
$$q_r'' = \varepsilon_d \left(\frac{1}{4}\int_{S^2} I(x,\omega)d\omega - \sigma T_d^4\right).$$

We need to complement the study with the analysis of the gas phase response in the vicinity of the droplet. This will be made with the quasi-steady state approximation and assuming spherical symmetry, leading to

$$\frac{1}{r^2}\frac{\partial}{\partial r}(r^2 v_g \rho_g) = 0 \ \ (\Rightarrow \rho_g v_g r^2 = \dot{m}), \tag{21}$$
$$\frac{1}{r^2}\frac{\partial}{\partial r}\left\{r^2\rho_g\left(v_g Y_{O_2} - \mathrm{D}_e\frac{\partial Y_{O_2}}{\partial r}\right)\right\} = -\frac{16}{27}w_2, \tag{22}$$
$$\frac{1}{r^2}\frac{\partial}{\partial r}\left\{r^2\rho_g\left(v_g Y_{AlO} - \mathrm{D}_e\frac{\partial Y_{AlO}}{\partial r}\right)\right\} = \frac{43}{27}w_2, \tag{23}$$
$$\frac{1}{r^2}\frac{\partial}{\partial r}\left\{r^2\rho_g\left(v_g Y_{Al} - \mathrm{D}_e\frac{\partial Y_{Al}}{\partial r}\right)\right\} = -w_2, \tag{24}$$
$$\frac{1}{r^2}\frac{\partial}{\partial r}\left\{r^2\rho_g\left(v_g c_p T - k\frac{\partial T}{\partial r}\right)\right\} = -q_2 w_2, \tag{25}$$

with $\rho_g = p/(\frac{\mathrm{R}}{M}T)$, and the corresponding boundary conditions (where the Clausius–Clapeyron relation is used):

- At $r = a$:

$$T = T_d, \tag{26}$$
$$Y_{Al} = Y_{Al}^s = \exp\left(\frac{L_v}{R_{Al}T_B} - \frac{L_v}{R_{Al}T_d}\right), \tag{27}$$
$$Y_{O_2} = 0, \tag{28}$$

  where L_v is the latent heat, $R_{Al} = \mathcal{R}/M_{Al}$ and T_B is the boiling temperature of aluminium at the ambient pressure.

- At $r \to \infty$:

$$T = T^g, \tag{29}$$
$$Y_\alpha = Y_\alpha^g, \ \ \alpha = Al,\, O_2,\, AlO. \tag{30}$$

By using the procedure introduced in Bermúdez et al[2, 3], different combustion models depending of the region (Ω_O or Ω_A) where droplet is gasifying could be derived. They would consist of

1. Ordinary differential equations for the time evolution of the radius and temperature of the droplet, given in terms of reaction rates.

2. Non-linear systems of equations, obtained by analysing the gas in the vicinity of the droplet, whose solutions provide us

   - Mass fractions of species and heat flux, at the surface of the droplet.
   - The position, r_f, of the diffusion flame.
   - Non-dimensional reaction rates.

3. Mass and energy sources from droplets to the "homogenised" gas phase.

3. Detailed model of particle creation

The previous section presented a model of droplet combustion that considered a vast cloud of droplets and how they interact. Central to this model was the concept that the combustion is controlled by the flow of oxygen from the far field and the flow of alumina gas from the droplet toward a flame front. This flame front has been taken to be infinitely thin by exploiting the high speed of the oxidation reaction and hence the flame occurs as the interface between an oxygen depleted region and an aluminium gas depleted region which is in the spirit of conventional diffusion flames. In this section we explore how the condensation may be controlled by thermal effects. Such behaviour will necessitate considering some finite-width flame effects. We still expect that the rapid combustion of gaseous aluminium will create a sharp interface between an oxygen depleted region and an aluminium gas depleted region. However, we need to consider a narrow region of combustion of $Al_{(g)}$ into $AlO_{(g)}$. Condensation into liquid Al_2O_3 droplets occurs later in the region 2 in Figure 5. In this region the condensation reaction will alter the concentration of oxygen as well as the concentration of gaseous aluminium oxide. Furthermore the condensation rate will alter with the size of the particles. The main rate controlling mechanism for condensation will be taken to be due to the highly exothermic nature of the condensation reaction so that the ability of a particle to exchange heat with its surroundings controls the rate of particle growth. Hence the diffusion flame model is extended to account for the particle behaviour and this creates a wide region at high temperature.

To develop and examine this model we consider the case of a single isolated droplet of aluminium with a radially symmetric flame surround it. Extending this to a more general situation has not yet been considered but might be done in a manner similar to earlier sections. At the inner edge of the flame the interface will be governed by a conventional diffusion flame criteria with both the fuel (aluminium gas) and the oxidant (oxygen) meeting and reacting so rapidly

that they both have zero concentration at the interface. This reaction at the interface produces gaseous aluminium oxide products which we generically call AlO (we have decided to include only one type of gaseous oxides species for simplicity). The model therefore has three distinct regions.

In region 1, between the droplet and the sharp interface, there is aluminium gas Al diffusing from the droplet surface, AlO diffusing from the interface but no O_2. There may also be liquid alumina particles Al_2O_3 which have diffused from region 2. We do not discuss the mechanisms that might create an oxide cap on the droplet surface and hence inhibit the evaporation and burning of the aluminium.

In region 2, outside this interface but in the flame, there will be aluminium gas AlO, liquid alumina particles Al_2O_3 and oxygen O_2. Finally in region 3, outside the flame, the temperature of the particles drops below the melting point and the condensation reaction turns off. A sketch of the three regions is shown in Figure 5.

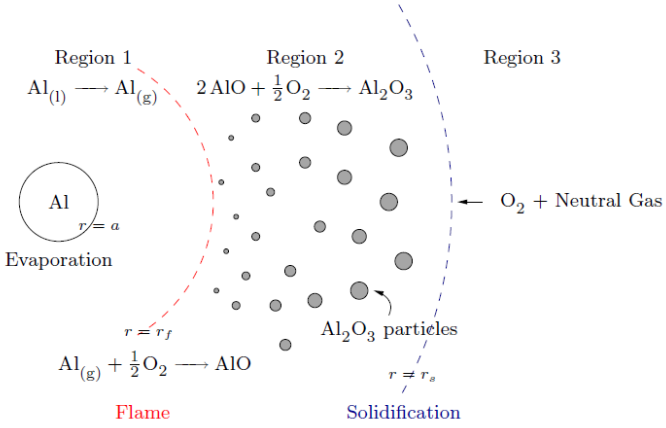

Figure 5: Sketch of the three regions.

In contrast to the earlier work in the interest of algebraic simplicity in this section we have neglected any effects due to gravity. This is justified in cases where the neutral gaseous species is very high in concentration. This neutral gas will therefore be nearly stationary and hence the other species and any particles simply diffuse in this gas.

We are going to look at particle creation around an evaporating aluminium droplet. We consider three regions:

- Droplet boundary: where aluminium evaporation takes place, $Al_{(l)} \rightarrow Al_{(g)}$. We may need to worry about an oxide cap forming on the surface of the aluminium droplet and possible deposition of alumina particles.

- Region 1: diffusion of $Al_{(g)}$ (no O_2) and AlO. Furthermore, alumina particles will probably not diffuse directly through the hot flame.
- Boundary between regions 1 and 2: flame with $Al_{(g)}$ and O_2 rapidly reacting.
- Region 2: liquid Al_2O_3 particle nucleation and growth, diffusion of O_2 and AlO (no $Al_{(g)}$)
- Boundary between regions 2 and 3: particle temperature drops below solidification point.
- Region 3: diffusion of O_2, neutral gas and solid particles.

3.1. Region 1

As before, let a be the radius of the aluminium droplet and r_f the position of the flame. The equations in region 1 are

$$\mathrm{D}_{Al}\nabla^2 Y_{Al} = 0, \tag{31}$$

$$k\nabla^2 T = 0, \tag{32}$$

in $r \in (a, r_f)$, where D_{Al} is the diffusion coefficient of $Al_{(g)}$, k is the thermal conductivity (of surrounding air), Y_{Al} is the number density of gaseous aluminium[1] and T is the gas temperature. At the droplet surface ($r = a$) we have the following boundary conditions

$$\mathrm{D}_{Al}\frac{\partial Y_{Al}}{\partial r} = M_B, \tag{33}$$

$$T = T_B, \tag{34}$$

where M_B is the source term coming from the boiling (mass being evaporated) and T_B is the boiling temperature of aluminium. The two boundary conditions are simplified versions of the free energy condition relevant at a liquid gaseous interface and are expected to be very accurate in this situation.

3.2. Region 2

At the interface between region 1 and 2, where the flame is, the following reaction takes place:

$$Al_{(g)} + 1/2O_2 -> AlO + \text{others?} \tag{35}$$

[1]The number density gives the number of aluminium particles per unit volume. It can be expressed in terms of the molar concentration c as $n = N_A c$ or the mass density ρ as $n = (N_A/M)\rho$, where N_A is the Avogadro's number and M is the molecular mass.

Accordingly, the boundary conditions at $r = r_f$ are

$$Y_{Al} = 0, \tag{36}$$

$$Y_{O_2} = 0, \tag{37}$$

$$T(r_f^+) = T(r_f^-), \tag{38}$$

$$\left[\rho c_p k \frac{\partial T}{\partial r}\right]_{r_f^-}^{r_f^+} = -2\mathrm{D}_{O_2} \frac{\Delta H_1}{N_A} \frac{\partial Y_{O_2}}{\partial r} = \mathrm{D}_{Al} \frac{\Delta H_1}{N_A} \frac{\partial Y_{Al}}{\partial r}, \tag{39}$$

where ΔH_1 is the reaction enthalpy of reaction (35).

Region 2 is where the reaction between the gaseous oxygen and gaseous aluminium oxides occurs to produce liquid alumina particles through the condensation reaction

$$2AlO + 1/2O_2 - > Al_2O_{3(l)}. \tag{40}$$

In this region this reaction causes (liquid) alumina particles to nucleate and grow. The equations in this region read

$$\mathrm{D}_{O_2} \nabla^2 Y_{O_2} = -\frac{1}{2} F, \tag{41a}$$

$$\mathrm{D}_{AlO} \nabla^2 Y_{AlO} = -2F, \tag{41b}$$

$$\rho c_p k \nabla^2 T = -\frac{\Delta H_2}{N_A} F, \tag{41c}$$

where Y_{O_2} and Y_{AlO} are number densities of O_2 and AlO, respectively, and D_{O_2} and D_{AlO} are their respective diffusion coefficients. The right-hand sides in these three equations account for the loss of molecules and heat because of the occurrence of reaction (40). The quantity F accounts for the amount of alumina particles being created per unit volume and unit time (thus F has units of number of particles/(m^3s)). The factors of 1/2 and 2 in the first two equations respectively are the stoichiometric coefficients. The right-hand side of (41c) gives the energy generated to produce a particle of Al_2O_3 (ΔH_2 is the energy released to produce a mole of Al_2O_3).

Here F will bridge between the macroscopic problem described in this section, and the microscopic problem for individual particles discussed in §3.4.

3.3. Region 3

The particles in Region 2 are assumed to be continually undergoing a reaction with the surrounding gases. However, this reaction turns off when the temperature of the particles drops below the solidification temperature of alumina. Taking this boundary to be at the point $r = r_s$ the boundary condition is:

$$Y_{AlO} = 0, \tag{42}$$

meaning that the reaction stops when there is no more fuel, as described by (42). This is likely to occur when the particles are liquid. This condition defines the interface between regions 2 and 3. In addition, we require continuity of O_2 and Al_2O_3 particles flux.

In region 3, O_2 concentration evolves according to

$$\mathrm{D}_{O_2}\nabla^2 Y_{O_2} = 0. \tag{43}$$

As we travel far from the droplet and the flame we expect that the surround gas will tend to a given temperature and the gas concentrations will settle to ambient conditions. Hence as $r \to \infty$ we have:

$$T = T^g, \tag{44}$$

$$Y_{Al_2O_3} = 0, \tag{45}$$

$$Y_{O_2} = Y^g_{O_2}. \tag{46}$$

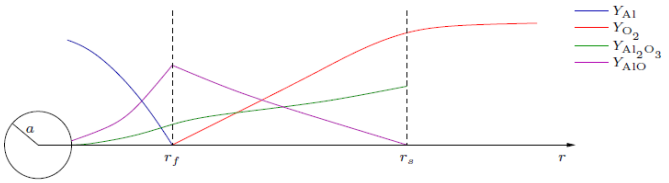

Figure 6: Sketch of the concentrations of each chemical species in the three regions.

3.4. Microscopic model

We now consider the details of how the particles nucleate and grow. We consider there to be a range of different particle sizes and look at how each of these might grow. To do this we will consider a micro problem of a single particle of alumina surrounded by gas of a given concentration.

Note that such a model of particle creation and growth can be employed to describe the resulting distribution of particle sizes that might be created when using the alternative manufacturing process where an Al-rich gas is created and then burnt by addition of oxygen.

Let $f(n, r, t)$ denote the number density of particles containing $n-$molecules of Al_2O_3 at radius r and time t (for simplicity, we use the number of molecules of Al_2O_3 to indicate the size of a particle, rather that its volume or radius). Nucleation brings about a reduction in free energy per unit volume, ΔG_v, which is balanced by the energy cost due to creation of new interface. Since the former scales like the particle's volume while the latter is proportional to

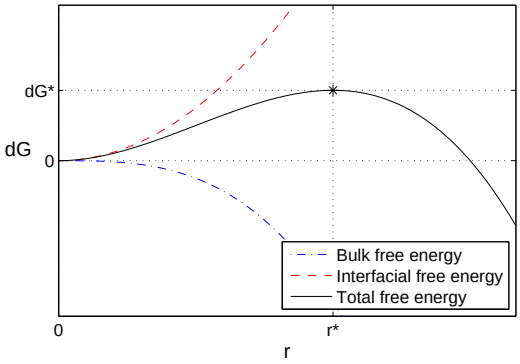

Figure 7: Bulk, interfacial and total free energy as a function of the radius. Shown with an asterisk is the free energy barrier ΔG^* after which nucleation is stable.

the particle's surface area, there is a critical particle size when the total free energy change is maximal, after which nucleation is favoured (see Figure 7). The total free energy is

$$\Delta G = \frac{4}{3}\pi r^3 \Delta G_v + 4\pi r^2 \kappa,$$

where κ is the interfacial surface energy. Then the critical free energy for nucleation is

$$\Delta G^* = \frac{16\pi\kappa^3}{3(\Delta G_v)^2}, \tag{47}$$

attained at the critical radius $r^* = -2\kappa/\Delta G_v$. Using the volume of a single molecule of alumina and assuming that the $n-$cluster is spherical we can relate r^* with n^* (the number of alumina molecules in a critical-size particle).

Only clusters above a critical size n^* are stable and exist (particle clusters below n^* molecules require more interfacial energy than volume free energy they release and are therefore unstable). The link between the microscopic quantity $f(n)$ and the macroscopic density $Y_{Al_2O_3}$ is given by

$$Y_{Al_2O_3}(r,t) = \int_{n^*}^{\infty} f(n,r,t) n \, dn. \tag{48}$$

The density f satisfies an advection-diffusion equation in the joint domain of cluster sizes and space,

$$\frac{\partial f}{\partial t} + \frac{\partial}{\partial n}\left(g(n) f\right) = \mathrm{D}_n \nabla^2 f, \tag{49}$$

where D_n is the diffusion coefficient of a $n-$cluster. If $\mathrm{D}_1 = \mathrm{D}_{Al_2O_3}$ is the diffusion coefficient of one alumina molecule, then using the Einstein relation for spherical particles we find that

$$\mathrm{D}_n = \frac{\mathrm{D}_1}{n^{1/3}}. \tag{50}$$

Note this relation is really only valid for liquid drops in low Reynolds numbers flows. Equation (49) tells us that an $n-$cluster will be "advected" towards larger clusters at a velocity $g(n)$ and spread with diffusion rate D_n (depending on its volume).

There is not a clear model for the growth rate $g(n)$ in the literature. Below we give a simple model obtained from a basic heat balance calculations around a particle. We assume that the heat of reaction is so large that upon nucleation the particle instantly reaches the dissociation temperature and then immediately to keep the particle at that temperature. We consider the following problem close to a cluster of radius R_n:

$$k\nabla^2\theta = 0, \qquad \text{in} \qquad r > R_n, \tag{51}$$

$$\theta = T_{\mathrm{diss}}, \qquad \text{at} \qquad r = R_n, \tag{52}$$

$$\theta = T^g, \qquad \text{as} \qquad r \to \infty, \tag{53}$$

where θ is the *microscopic* gas temperature, T_{diss} is the dissociation temperature (temperature above which alumina would dissociate into its components following the reverse of reaction (40)). We assume that the cluster is at this temperature since as nucleation proceeds, the temperature of the cluster could potentially increase since energy is released as it grows (for $n > n^*$), but never above T_{diss}. Here T refers to the macroscopic gas temperature (which is the one *one sees* and that we have used so far) far away from the cluster. Solving this we find that $\theta = (T_{\mathrm{diss}} - T)R_n/r + T$.

We are interested in the heat flow at the surface of the $n-$particle cluster. This can be expressed as

$$\rho c_p k \frac{\partial\theta}{\partial r} 4\pi r^2 \quad \text{at} \quad r = R_n.$$

Substituting in the expression for $\theta(r)$ and $R_n = R_p n^{1/3}$ we find that

$$\rho c_p k 4\pi R_p n^{1/3}(T_{\mathrm{diss}} - T).$$

This is the heat flux per $n-$cluster. To relate this with the growth rate $g(n)$ (molecules per second) of a $n-$cluster, we simple divide the above expression by the energy required to produce a molecule of Al_2O_3, given by $\Delta H_2/N_A$,

$$g(n) = \frac{N_A}{\Delta H_2}\rho c_p k 4\pi R_p n^{1/3}(T_{\mathrm{diss}} - T), \tag{54}$$

where R_p is the radius of one molecule of alumina and accordingly $R_p n^{1/3}$ is the radius of a $n-$molecule cluster.

The amount of alumina being created (F in (41)) has two components. First, some n^*-clusters will appear at a rate I, known as the nucleation rate. This rate is given by the classical steady-state equation (see McPherson[6])

$$I = A \exp\left(\frac{-\Delta G^*}{k_B T}\right), \tag{55}$$

where k_B is the Boltzmann's constant. McPherson[6] points out "that A may be regarded as a constant because of the preponderance of the exponential term ΔG^*. There is considerable uncertainty in the preexponential term A but this is relatively unimportant compared with the large changes in the exponential term produced by small temperature changes".

Second, one must take into account the growth of $n-$clusters with $n > n^*$. If we define $g(n)$ to be the growth rate of a particle-cluster of size n, then the total rate of production of alumina reads

$$F = I + \int_{n^*}^{\infty} g(n) f(n)\, dn. \tag{56}$$

Combining (49), (54) and using (55) as a boundary condition, we obtain a closed expression for $F(r,t)$ in (56), which we can then plug back into (41).

4. Conclusions

A procedure to derive a model taking into account the vaporisation, combustion and further nucleation to form alumina particles, was introduced. It combines infinitely fast gas phase oxidation reaction of aluminium with finite rate condensation controlled by thermal effects.

References

[1] M.W. Beckstead, A Summary of Aluminum Combustion, Paper presented at the RTO/VKI Special Course on "Internal Aerodynamics in Solid Rocket Propulsion", held in Rhode-Saint-Genèse, Belgium, 27-31 May 2002, and published in RTO-EN-023

[2] A. Bermúdez, J.L. Ferrín and A. Liñán, The modelling of the generation of volatiles, H_2 and CO, and their simultaneous diffusion controlled oxidation, in pulverized coal furnaces, *Combusion Theory and Modelling*, **11(6)** (2007) 949-976.

[3] A. Bermúdez, J.L. Ferrín, A. Liñán and L. Saavedra, Numerical simulation of group combustion of pulverized coal, *Combustion and Flame*, **158(9)** (2011) 1852-1865.

[4] A. Liñán. The asymptotic structure of counterflow diffussion flames for large activation energies. *Acta Astronáutica*, **1** (1974) 1007-1039.

[5] A. Liñán. Theory of droplet vaporization and combustion. In R. Borghi, P. Clavin, A. Liñán, P. Pelcé, and G.I. Sivashinsky, editors, *Modélisation des Phénomèmenes de Combustion*, Paris, 1985. Eds. Eyrolles.

[6] R. McPherson, Formation of metastable phases in flame- and plasma-prepared alumina, *Journal of Materials Science*, **8(6)** (1973) 851–858.

[7] C.V. White, O. Mikkelsen and D. Roha, Status of the Alcoa Carbothermic Aluminum Project, in International Smelting Technology Symposium: Incorporating the 6th Advances in Sulfide Smelting Symposium (eds J. P. Downey, T. P. Battle and J. F. White), John Wiley & Sons, Inc., Hoboken, NJ, USA (2012). doi: 10.1002/9781118364765.ch10

Designing an optimal network measurement sensors for monitoring geographical renewable resource

Academic Coordinators Manuel Febrero
University University of Santiago de Compostela and Technological Institute for Industrial Mathematics

Business Coordinator Martín Gastón
Company Centro Nacional de Energías Renovables (CENER)

Team Mario Santoro, Manuel Oviedo, Wonju Jeon, Chulmin Kang, Iria Roca, Lino Álvarez, Aurea Martínez, Iván Moya, Giorgi Khimshiashvili, María José Ginzo

Designing an optimal network measurement sensors for monitoring geographical renewable resource

Manuel Febrero Bande [*], *Martín Gastón Romeo* [†]

Abstract

This document analyses how a network of sensors can be designed in order to be optimal in the sense that represent the data closer as possible minimizing the uncertainty.

1. Challenge description

The National Renewable Energy Centre (CENER) is a public institution that pretends to be a research centre of excellence in the renewable energies field with international outreach. One of aims of CENER (related with solar resource characterization) is to generate solar resource maps using satellite databases and manage remote monitorization campaigns that can be the foundation for establishing a network of sensors in the ground that characterizes the amount of solar resource available. This is the goal of this paper: Design a network of sensors from the information obtained from remote monitorization and satellite databases for the solar field characterization. This task would be specially useful in under developed areas where no ground data is available as a previous task for installing a initial network of sensor identifying the most suitable points to install a ground station to collect the resource information.

2. Data

Along this paper, we will use a database of solar resource of Iberian peninsula obtained from satellite data with the goal of designing the optimal network of sensors. Also along this paper, we will consider that the number of sensors in known in advanced, i.e. our aim is to put n sensors optimizing its location.

[*]University of Santiago de Compostela and ITMATI; manuel.febrero@usc.es
[†]Centro Nacional de Energías Renovables (CENER)

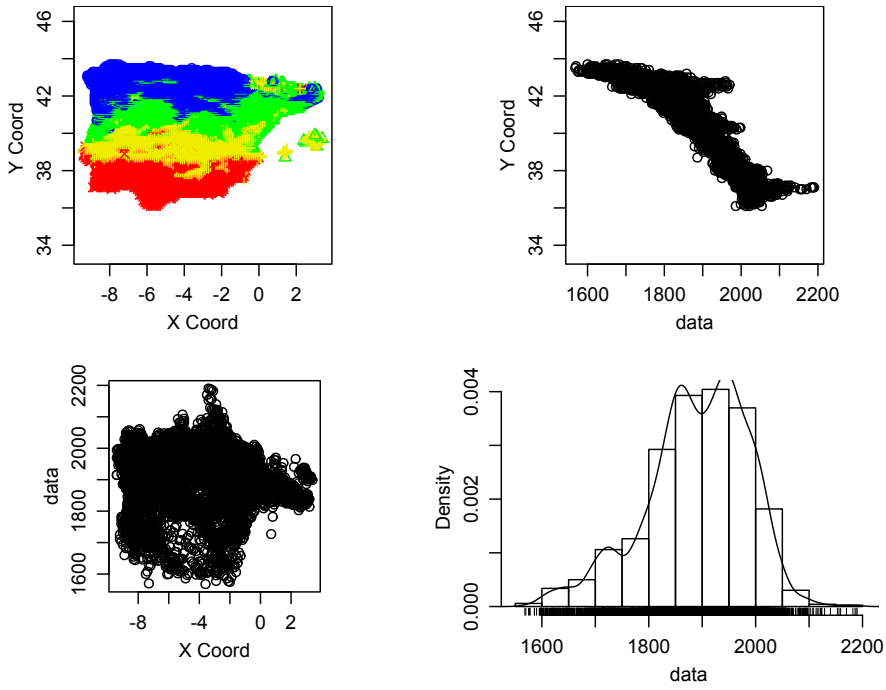

Figure 1: Geostatistical analysis of solar resource in Spain

The first task is to analyze the data from the geostatistical point of view. The design of a optimal network is related with minimizing the variance of our estimator which is a kriging estimate of the solar resource here represented by a Solar Radiation Index (SGHI). So, in order to estimate the variance, the systematic effects related with the mean have to be removed. Figure 1 shows classics geostatistics exploratory data analysis of the solar resource using the `geoR` library (see [1]). The up-left figure is showing the pattern of the solar resource by colors from blue (low) to red (high). There is a clear latitude pattern which is confirmed in the up-right figure where only the effect of the latitude (Y Coord) is represented respect to data. The shape in this figure shows the expected pattern that the south has more solar radiation than the north. There is no effect on longitude as can be seen in bottom-left figure. Finally, in bottom-right figure, the histogram of the data is represented. The data is slightly skewed to the right.

The next step is to remove the effect of the latitude on the resource. Typically, this is done establishing a regression model of those influential variables respect to the model. In this case, we use a non parametric model of the form

$$SGHI_s = s(lat) + \epsilon_s$$

where s is a smooth function.

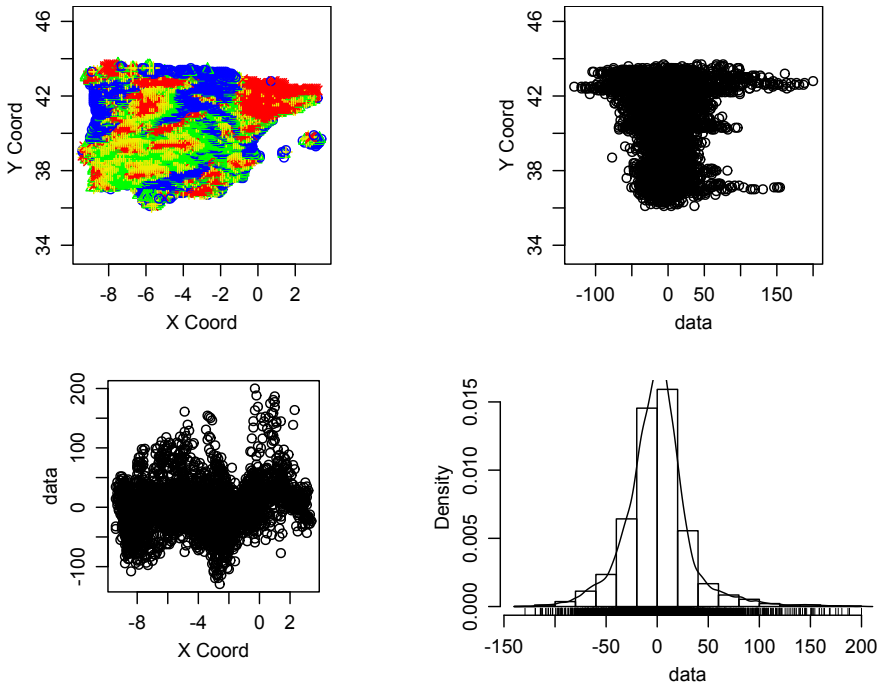

Figure 2: Residuals of SGHI after removing the latitude effect

The results are plotted in Figure 2 where now no pattern is detected from latitude or longitude. Indeed, the residuals seems to be symmetric and unimodal. Now, the data is prepared to analyse the variance using a variogram. The variogram is the fundamental tool in kriging to describe the spatial covariance. For a detailed introduction in Geostatistics, see [2].

Basically, the variogram in direction h is defined as:

$$\gamma(h) = \frac{1}{2}\mathrm{V}S(x) - S(x+h)$$

and its related with spatial covariance through $\gamma(h) = \mathrm{V}0 - \mathrm{V}h = \sigma^2\{1-\rho(h)\}$ where σ^2 is the variance of the process and ρ is the spatial correlation. A typical assumption here is that the spatial process is intrinsic, i.e. the variogram depends only in distance and not in direction $\gamma(h) = \gamma||h||$. Indeed, the variogram of a observation process usually adds the measurement variance, denoted by τ^2. With these conditions, a typical variogram is a monotone increasing function with the following features. The intercept, τ^2, corresponds to the *nugget* variance (measurement error variance). The asymptote, $\tau^2+\sigma^2$, corresponds to the variance of the observation process, sometimes called the *sill* (the sum of the nugget and the signal variance). The shape in which the variogram increases from its intercept to its asymptote is determined by the correlation function ρ. The most important features of ρ are closed to zero ($\rho(0)$) and how quickly this function approaches to zero with a increasing h.

That point h_r such that $\rho(h) = 0, h >= h_r$ is called the *range* of the variogram and establish the end (in distance) of the spatial dependence.

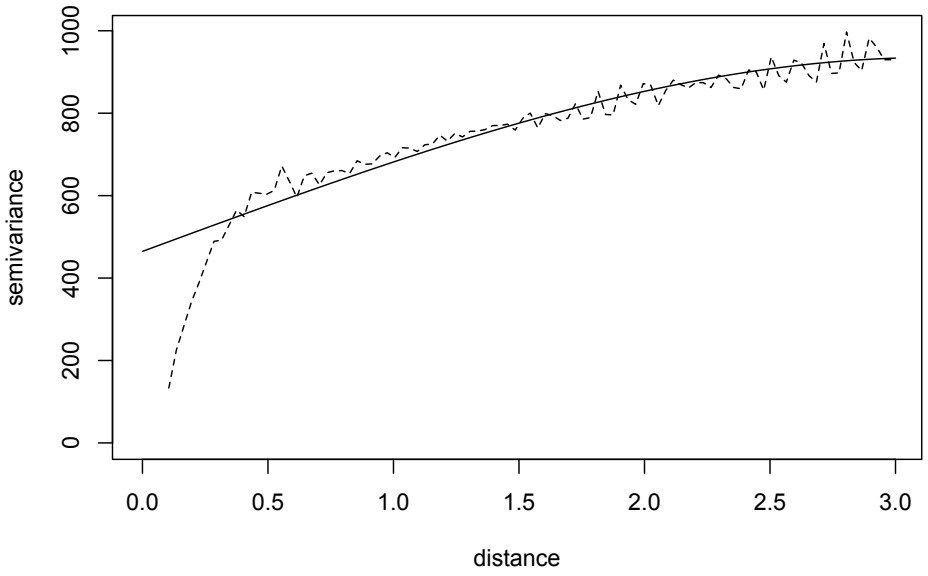

Figure 3: Variogram of residual data

Figure 3 shows the adjust of spherical model to the empirical variogram. For this example, $\tau^2 = 464.692$, and $\sigma^2 = 470.366$ and the range is $h_r = 3.143$. These parameters give the amount of variance that it is explained when a sensor is located at a certain point. Near the point, the variance decrease 50.3034% and the influence is lost at distances greater than h_r. The variogram could be considered as a reference of the amount of variance that should be explained where a sensor is located at a certain point. So, the rest of the paper is devoted to estimate the variance surface and to consider several strategies for selecting the network grid reducing the total amount of variance.

3. Variance surface

Using again the whole dataset along one year, the mean and the variance at each location point can be estimated. This is shown in Figure 4 where the mean surface shows the expected trend from south to north. The variance surface shows several local features that surely depends on orographic details. The variance is higher in the north-west quadrant and there are some up-and-downs near the Pyrenees.

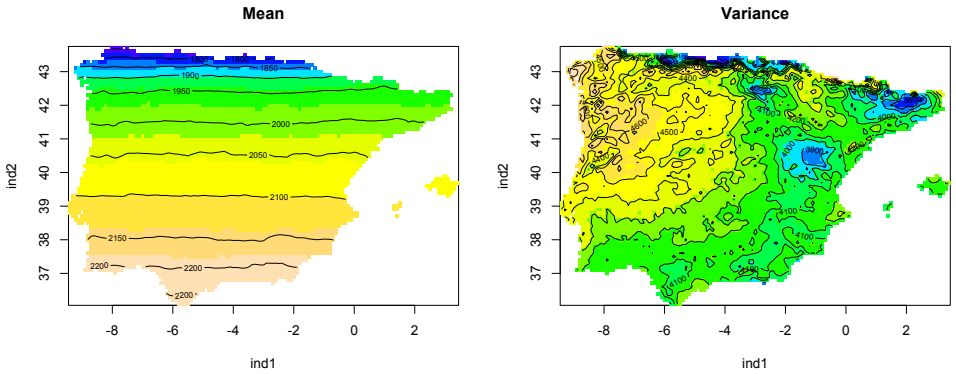

Figure 4: Mean and Variance estimated along one year

The variance surface is too wiggly to implement a reasonable choice of the network so, we decided to smooth it to have a more consistent selection. The effect of the smoothing is shown in Figure 5. This would be our starting point for the subsequent strategies.

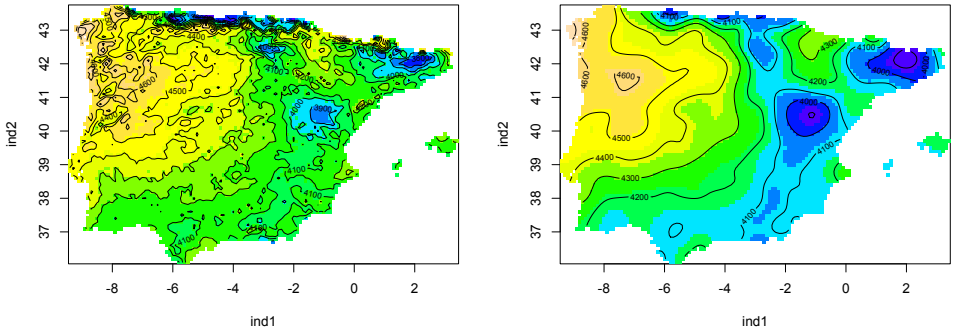

Figure 5: Original (left) and smoothed (right) variance surface

4. Strategies for selecting locations

In the following several strategies are considered to select the network grid. Basically, all of them selects a point, then downscale the variance surface according with the spatial dependence given by the variogram and so on. The strategies differ on practical restrictions over the points. For simplicity, we consider $n = 15$ the number of stations to be located.

Option 1.

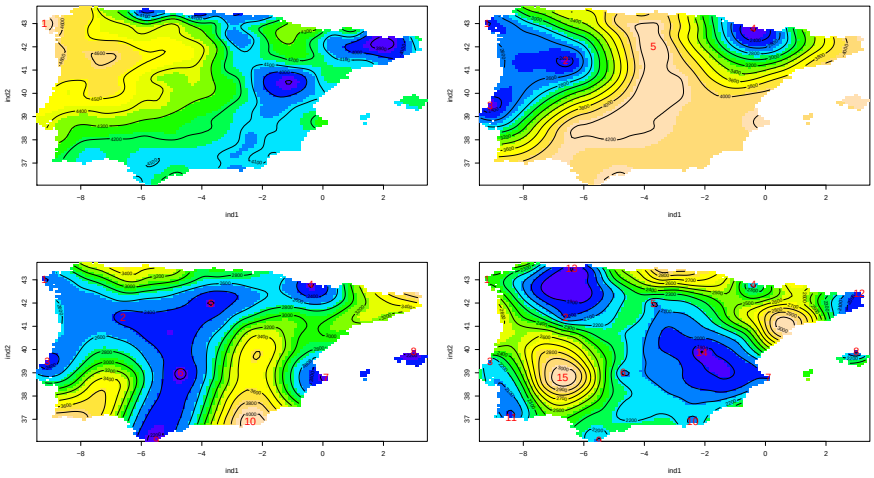

Figure 6: Intermediate results using Strategy option 1

The first idea was to put the stations on that point with maximum variance. The final result along with intermediate steps at (1,5,10) are shown in Figure 6 where the order of the locations are plotted with a number in red. The first station is located in the Galicia coast and subsequent stations have the tendency to be located at the border of the map. In the final result, ten stations are located in the border and only five in the interior of Iberian Peninsula.

Option 2.

To avoid the undesirable effect that the majority of the stations where located at the coast, we impose a practical restriction that the station should be located 0.3 (in degrees) inside the map following after this the same procedure as option 1. The result is plotted in 7 jointly with the smoothed original variance. Now, the locations are not in the coast but in the new border fulfilling the restriction. So, this option does not solve the problem of the first one.

Option 3.

Finally, the third option tries to minimize the overall decrease in the variance surface. Every time a new location is selected, it produces a downscaling of the variance in the vicinity and this option takes into account the sum of all of these downscales. This option is clearly the most heavy in terms of computing because to decide a new location we must try with all of them in every step. Nevertheless, the option seems to work fine selecting in the first steps locations in the inner part of the map. The main drawback of this approach is that after the ten first locations, new ones are located close to the previous ones. But additional restrictions could be impose over the network as for instance, a minimum distance between sensors. The final result jointly with intermediate steps are shown in Figure 8.

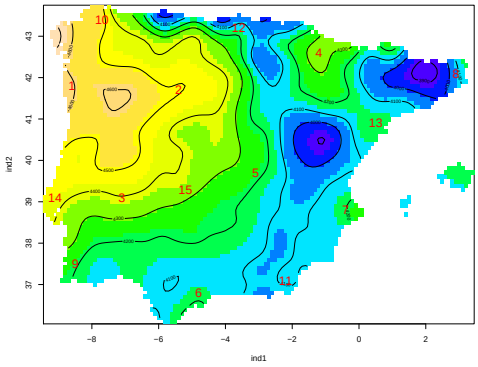

Figure 7: Network grid locations for Option 2 with original variance

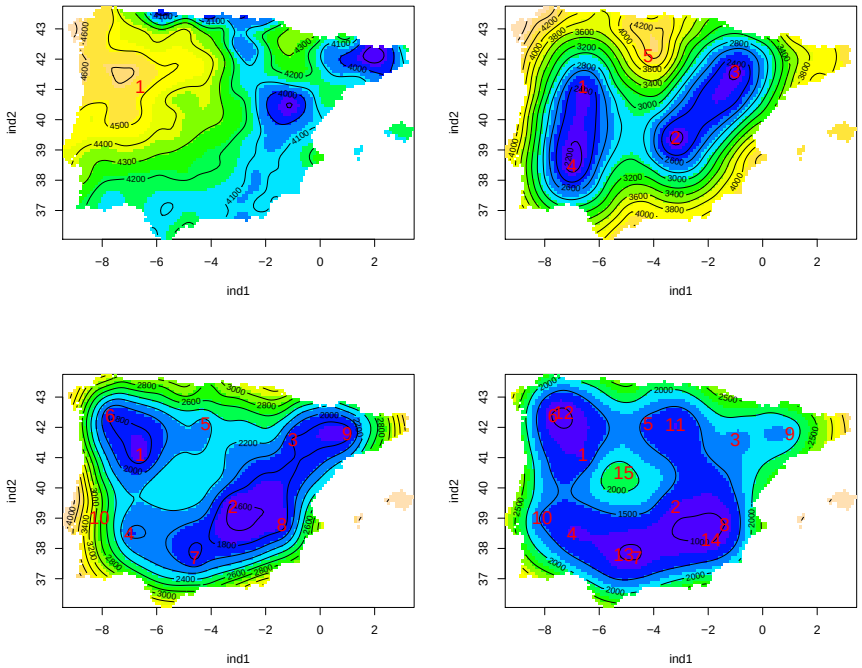

Figure 8: Intermediate results using Option 3

5. Conclusions

In this paper, a method for selecting ground locations where to establish measurement stations is presented. The key idea of this method is to use the variance surface of the remote monitoring data to find those sites with higher variance which will be the candidates to be included in the network. Once a location is included, the variance is downscaling in the vicinity according with the estimated spatial dependence detected in the remote monitoring data. During the sessions of the study groups, three options were proposed using different criteria. Of course, many others can be also proposed and the final choice is a matter of convenience that can also take into account other practical and/or subjective considerations.

References

[1] P. J. Ribeiro Jr and P. J. Diggle, "geoR: A package for geostatistical analysis," *R news*, vol. 1, no. 2, pp. 14–18, 2001.

[2] P. Diggle and P. J. Ribeiro, *Model-based geostatistics*. Springer, 2007.

Acknowledgements

The Scientific Committee wishes to thank the company speakers, the academic coordinators and the researchers of each working team for their invaluable contributions to the scientific success of the 97 European Study Groups with Industry.

We also want to express our gratitude to Teknova AS that through a project funded by the Norwegian government has supported both scientific and economic fronts of this event. We would also like to thank to the Faculty of Mathematics of the University of Santiago de Compostela which held the 97 ESGI.

Finally, we would also like to express our gratitude to ITMATI's Manager, Rubén Gayoso, the Technology transfer and innovation manager of ITMATI, Adriana Castro, researcher of the Department of Statistics and Operations Research, María José Ginzo-Villamayor, and the Technology translator of math-in, Guadalupe Parente, whose meticulous work and dedication have contributed to the success of this 97 ESGI.